Realia et naturalia

DISSERTATIONES
PHYSICAE
UNIVERSITATIS
TARTUENSIS
100

KARLIS ZALITE

Radar Remote Sensing for Monitoring Forest Floods and Agricultural Grasslands

DISSERTATIONES PHYSICAE UNIVERSITATIS TARTUENSIS
100

DISSERTATIONES PHYSICAE UNIVERSITATIS TARTUENSIS
100

KARLIS ZALITE

Radar Remote Sensing for Monitoring Forest Floods and Agricultural Grasslands

UNIVERSITY OF TARTU
PRESS
1632

This study was carried out at the University of Tartu, and Tartu Observatory, Estonia.

The dissertation was admitted on December 18, 2015, in partial fulfilment of the requirements for the degree of Doctor of Philosophy in physics, and allowed for defense by the Council of the Institute of Physics, University of Tartu.

Supervisors:	DSc Mart Noorma, University of Tartu, Estonia PhD Kaupo Voormansik, Tartu Observatory, Estonia PhD Anu Reinart, Tartu Observatory, Estonia
Opponents:	Dr Juan Manuel Lopez-Sanchez, University of Alicante, Spain Dr Rivo Uiboupin, Tallinn University of Technology, Estonia
Defense:	January 26, 2016, University of Tartu, Estonia

This research was supported by the European Social Fund's Doctoral Studies and the Internationalisation Program DoRa.

ISSN: 1406-0647
ISBN: 978-9949-77-024-3 (print)
ISBN: 978-9949-77-025-0 (pdf)

University of Tartu Press
www.tyk.ee

CONTENTS

NOMENCLATURE

List of acronyms

C-band	Frequencies from 4 GHz to 8 GHz
CSK	COSMO-SkyMed
EM	Electromagnetic
ENL	Equivalent number of looks
ESA	European Space Agency
HH	Horizontal send, horizontal receive
HV	Horizontal send, vertical receive
InSAR	Interferometric synthetic aperture radar
L-band	Frequencies from 1 GHz to 2 GHz
NEBN	Noise Equivalent Beta Nought
NESZ	Noise Equivalent Sigma Zero
PolSAR	Polarimetric synthetic aperture radar
R2	RADARSAT-2
RMS	Root mean square
SAR	Synthetic aperture radar
SNR	Signal-to-noise ration
TDX	TanDEM-X
TDX/E	TanDEM-X evening pass
TDX/M	TanDEM-X morning pass
UTC	Coordinated Universal Time
VH	Vertical send, horizontal receive
VV	Vertical send, vertical receive
X-band	Frequencies from 8 GHz to 12 GHz

List of symbols

α	Dominant scattering alpha angle
$\bar{\alpha}$	Mean scattering alpha angle
γ	Complex interferometric coherence
γ_{hhvv}	HH/VV coherence
$\gamma_{T_{12}}$	T_{12} coherence
γ_{total},γ_v,γ_t,γ_{SNR},γ_{bias}	Total coherence, and its separate contributions
Δ	Orientation randomness parameter

θ_i	Angle of incidence
κ_z	Vertical wavenumber
λ	Wavelength
σ^0	Backscattering coefficient
σ_c^0,σ_m^0,σ_t^0,σ_s^0,σ_d^0	Scattering mechanisms
σ_{rms}	RMS motion of scatterers in the resolution cell
A	SAR polarimetric anisotropy
A_p	Particle anisotropy
a,b	Real and imaginary parts of a complex number
B_n	Perpendicular baseline
f_V	Intensity of the vegetation volume scattering
i	Imaginary unit
H	SAR polarimetric entropy
h, h_v	Vegetation height
h_a	Height of ambiguity
R	Range to target
$ratio_{hhvv}$	HH/VV channel intensity ratio
r	Correlation coefficient
S_{qp}	Scattering matrix element
s_x	Complex image value
T_{xy}	xth row, yth column element of the coherency matrix **T**
t	Temporal baseline

LIST OF ORIGINAL PUBLICATIONS

This thesis is based on the following publications (full texts included at the end of the thesis), which are referred to in the text by their Roman numerals. The papers are reprinted with the kind permission from the publishers.

I **K. Zalite**, K. Voormansik, A. Olesk, M. Noorma and A. Reinart, *Effects of Inundated Vegetation on X-Band HH-VV Backscatter and Phase Difference*, IEEE Journal of Selected Topics in Applied Earth Observations and Remote Sensing, vol. 7, no. 4, pp. 1402–1406, 2013.

II **K. Zalite**, O. Antropov, J. Praks, K. Voormansik, M. Noorma, *Monitoring of Agricultural Grasslands with Time Series of X-band Repeat-Pass Interferometric SAR*, IEEE Journal of Selected Topics in Applied Earth Observations and Remote Sensing, vol. PP, 2015.

III K. Voormansik, T. Jagdhuber, **K. Zalite**, M. Noorma, I. Hajnsek, *Observations of Cutting Practices in Agricultural Grasslands using Polarimetric SAR*, IEEE Journal of Selected Topics in Applied Earth Observations and Remote Sensing, vol. PP, 2015

IV **K. Zalite**, O. Antropov, J. Praks, K. Voormansik, M. Noorma, *Towards detecting mowing of agricultural grasslands from multi-temporal COSMO-SkyMed data*, 2014 IEEE International Geoscience and Remote Sensing Symposium (IGARSS), pp. 5076–5079, 2014.

Author's contribution to the publications

Author's research has given an essential contribution to all these publications. Here the author's contribution to the original publications is indicated. The Roman numerals correspond to those in the list of publications.

Publication I. The author performed the calculations of the microwave backscatter and polarimetric phase difference. He designed the structure of the paper, prepared all the figures, and did most of the writing. He is responsible for the interpretation of the results, in cooperation with Kaupo Voormansik.

Publication II. This work is an elaboration on the study done in Publication **IV**. The author designed the structure of the paper, and was responsible for all the processing and calculations presented there. Interpretation of the results was done

jointly with Oleg Antropov, Jaan Praks, and Kaupo Voormansik. Majority of the paper was written by the author.

Publication III. This work was a collaborative effort. The author was responsible for the modeling using the vegetation particle scattering model, and for implementing the modified Freeman decomposition. The author also contributed in the interpretation of the results, and was involved in the writing and formatting of the article.

Publication IV. This work presents the preliminary results, and the study continues in Publication **II**. The author performed all the processing and prepared the conference article with the help of Jaan Praks and Oleg Antropov.

1. INTRODUCTION

1.1. Background

Remote sensing lies naturally on the path of humankind's technological advance. Gaining more information about the widest possible area on Earth is key to a variety of applications, be it military reconnaissance or prediction of harvest. The aforementioned objectives are met by raising the observation platform in order to cover a larger area, and by using more sophisticated and precise instruments. Invention of the camera in the first half of the 19th century marks the beginning of the modern remote sensing. Balloons and kites served as the first platforms during the attempts to apply this new technology to land survey and reconnaissance. Military applications remained prevalent as airplanes became the dominant observation platform during the beginning of the 20th century. However, one of the first artificial satellites put into orbit – Vanguard 2 – is recorded in history as the first meteorological satellite [1]. Furthermore, the design of the Earth Resources Technology Satellite [2] in the 60s and 70s focused on many remote sensing applications, e.g. agriculture/forestry, environmental quality/ecology and others [3]. The satellite was launched in 1972, and later renamed to Landsat – the first of a successful remote sensing satellite series.

The 1970s also saw the launch of the first civilian Synthetic Aperture Radar (SAR) satellite Seasat [4, 5]. SAR is rooted in the radar technology – invention of the World War II era. A decade after the end of the war the first principles of obtaining two-dimensional images of the Earth's surface from radar signals were postulated [6, 7]. It took almost three more decades for the technology to allow the launch of Seasat in 1978. To obtain feasible resolution, the beam aperture had to be synthetically increased in the azimuth direction, differentiating SAR from the real aperture systems [8]. This required complex signal processing, limiting the implementation of SAR in the early years of its development [9, 10]. The following decade featured Shuttle-based SAR systems (with the exception of Soviet 1870 SAR [11]) – SIR-A [12] and SIR-B [13]. Both of these systems were based on the L-band (frequencies from 1 GHz to 2 GHz) HH polarization (horizontal send, and horizontal receive) radar used on Seasat [14].

Data from the Seasat mission were used in numerous studies. The single-polarization L-band imagery was used to create high-precision maps of sea ice motion [15], as well as to determine and map sea ice velocity [16]. Foundations for oil spill detection were established as well [17]. The data were also used to develop classification and segmentation techniques based on the speckle [18, 19]. Furthermore, Seasat demonstrated the capabilities of space borne Interferometric SAR (InSAR – study

of phase differences between at least two complex-valued SAR images [20]) systems [21, 22]. Due to a power failure, the Seasat mission ended after a little more than three months following the launch. However, as mentioned before, the same radar was used on SIR-A and SIR-B missions aboard the Shuttle, providing further data for research and development of applications. Research into surface penetration first reported for Seasat by Blom *et al.* in 1984 [23] continued for SIR-A and SIR-B [24, 25], giving insight into radar remote sensing of complex environments with multi-layered structure. Furthermore, radar backscatter from biomass was extensively studied, including multi-frequency and multi-polarization data from SIR missions and airborne radars. Ability of L-band radar signal to penetrate dense biomass was reported [26], and relation of the returned signal to the biomass amount and tree height was shown [27, 28]. In [27], Wu also reported higher backscatter of X-band (frequencies from 8 GHz to 12 GHz) HH signal from forests with standing water beneath the canopy – a similar effect reported previously by MacDonald *et al.* for L-band in [29]. Studies also focused on agricultural applications, investigating the response of the L-band HH radar to variable soil moisture and roughness conditions [30]. In addition, dependence of the returned signal on the biomass and state of the agricultural vegetation cover was demonstrated [31, 32, 33].

The next Shuttle SAR mission was SIR-C/X-SAR [34] in 1994. It provided a very comprehensive data set: L-, and C-band (frequencies from 4 GHz to 8 GHz) in HH, HV (horizontal send, vertical receive), VH (vertical send, horizontal receive), and VV (vertical send, vertical receive) polarizations (further – quad- or full-pol), as well as X-band in VV polarization. It followed the launch of C-band single polarization (further – single-pol) VV ERS-1 [35] and L-band single-pol HH JERS-1 [36] satellites. In 1995, two additional satellites were launched – C-band single-pol VV ERS-2 [37] and C-band single-pol HH RADARSAT-1 [38]. In 2002, the European Space Agency's (ESA) Envisat was launched with the dual-pol (providing up to two combinations of polarization in a data set) C-band radar on board [39]. The availability of data allowed to develop and refine many information retrieval algorithms, and techniques for the space borne SAR data, including InSAR and polarimetric SAR (PolSAR – study of how the returns of differently polarized radar signals depend on the properties of the sensed object, i.e. structure, orientation, dielectric properties and surface roughness). While studies related to the polarization of electromagnetic (EM) radiation date back to the beginning of the 19th century [40], Boerner established the foundations of PolSAR [41] based on the fundamental work done by Sinclair [42], Kennaugh [43] and Huynen [44]. The first permanent quad-pol SAR satellite was launched into orbit in 2006 – it was the ALOS-PALSAR radar operating in L-band [45].

Starting with 2007, a different era started for the space borne SAR systems – their

development was driven by user requirements rather than by technology [46]. Higher spatial resolution and multiple operational modes meant that previously impossible applications could be developed. The first to represent the new era was quad-pol C-band RADARSAT-2 [47] and X-band TerraSAR-X [48], both launched in 2007. The latter was joined by an identical TanDEM-X mission in 2010 [49], and the two satellites now fly in formation. Furthermore, in 2010, a constellation of four X-band dual-pol SAR satellites was completed, named COSMO-SkyMed [50]. In 2014, ESA launched its first Copernicus programme satellite Sentinel-1 [51] operating in C-band in dual-pol mode.

Availability of sophisticated space borne SAR instruments covering multiple frequencies and combinations of signal polarization allow for the development of remote sensing techniques for complex, composite environments. Two such environments are flooded forests and agricultural grasslands – the focus of this thesis. Monitoring of these environments is important for several reasons. Floods are one of the most damaging natural hazards. In Europe, up to 75% of all insurance claims are from flood damage [52]. Due to its impact on the nature and communities, flood mapping is a fairly established remote sensing topic, be it with optical or SAR instruments [53]. SAR plays an essential role in flood mapping as the radar signal can penetrate the clouds that often cover the flooded area [54]. Additionally, SAR can also penetrate the forest canopy thus giving the opportunity to map floods in forested areas as well [55]. Besides destruction of infrastructure, forest floods cause specific environmental damage and make the monetary estimation of the damage problematic [56]. However, damage to the ecosystem is profound. Kozlowski [57] and Coder [58] list several major effects of forest flooding, including emission of greenhouse gases, decline of tree growth, and soil erosion, among others.

As mentioned before, already in 1980 MacDonalnd *et al.* [29] reported anomalously high radar returns for the L-band Seasat from certain forested areas, later identified as areas having of standing water under the canopy. Later Ormsby *et al.* [59] reported a 3 dB to 6 dB increase of backscattering coefficient over areas of flooded forests when compared to non-flooded cases for the L-HH (L-band, HH polarization). Using the SIR-C data, Hess *et al.* [60] reported similar results, i.e. an increase of about 3 dB for L-HH and less for other combinations (C-HH/HV/VV, L-HV/VV). Hess *et al.* [60] also calculated phase differences between C-HH and C-VV, as well as between L-HH and L-VV. For the L-band case, the phase difference was offset from 0° for non-flooded forest toward 180° for the flooded case. The phase difference is evidence of the double-bounce scattering mechanism [61]. Flooded forests are composite environments where the received signal may have several sources of scattering, including the double-bounce between the trunk and the surface [62, 63, 64]. Pope *et al.* [65] showed that the HH–VV phase difference is the parameter with one

of the most pronounced changes due to flooding, suggesting its potential use in flood mapping applications. The effects of increased backscatter and HH–VV phase difference due to flooding of forests, however, vary with frequency, polarization, and incidence angle, as well as particular forest characteristics [66, 67]. While steeper incidence angles are preferred for backscatter-based flood mapping [68], the HH–VV phase difference increases with increasing incidence angles [69, 70]. Longer wavelengths are usually preferred due to less attenuation in the forest canopy and larger interaction with the trunk and ground [71]. However, Voormansik *et al.* [68] successfully demonstrated the capability to delineate forest floods using X-HH TerraSAR-X, thus opening the possibility to create flood mapping applications based on this high-resolution instrument.

Agricultural grasslands is another complex environment where remote sensing can play a large role in the future operational applications. Grasslands constitute a significant part of Europe's agricultural area [72], and they play a large role in production of livestock, tourism, maintaining biodiversity, and protection form soil erosion [73]. Remote sensing of agricultural areas is a well established topic [74, 75, 76, 77], and SAR is playing an increasing role in their monitoring [78, 79, 80]. Researchers of agriculture, including grasslands, have mainly dealt with classification of grasslands and their distinction from other land cover types, monitoring of management practices, and characterization of the vegetation present on the field. However, certain topics regarding agricultural grasslands have been covered relatively lightly. For example, while classification of vegetation is well studied for crops as well as grasslands [81, 82, 83], estimation of biomass and detection of management practices on agricultural grasslands is not researched as well as in the case of crops [84, 85, 86]. However, due to their economic and environmental importance, agricultural grasslands would benefit greatly from the application of newest SAR remote sensing techniques. As an example, one could mention the verification of subsidy claims of farmers in the EU regarding certain agricultural practices aiming at maintaining the biodiversity of grasslands [87].

Characterization of grassland vegetation, and detection of agricultural management practices could be achieved from the perspective of both PolSAR and InSAR. Techniques reported for agricultural crops can be partially applied to grasslands as well. Vegetation height and management practices are similar, but a possible mix of plant species on grasslands can introduce significant differences. In the case of PolSAR, success has been reported in relating grass height to backscatter for different polarizations [88, 89]. Limited success is reported on the topic of detection of management practices [90, 85, 86]. However, in a study by Voormansik *et al.* [91], no reliable X-band HH/VV PolSAR indicator separating tall and short grass was found, possibly due to a limited data set. On the other hand, several parameters

were found the be sensitive to mowing events in the case when grass was left lying on the field [91]. As for InSAR, relation between interferometric coherence and height of tall vegetation is well established [92, 93, 94]. However, in the case of crops and grasslands, the number of studies is limited due to decorrelation effects [95, 80]. Techniques based on the repeat-pass interferometric coherence can also be applied to the detection of mowing events as removal of vegetation would, in principle, increase the interferometric coherence. Up to date, however, there are no operational applications developed using SAR for monitoring of agricultural grasslands. Therefore, novel PolSAR and InSAR approaches could be investigated in order to support the future implementation of such applications.

1.2. Objectives and progress of this work

The objective of this work is to investigate the use of advanced InSAR and PolSAR techniques and high quality data sources for monitoring of two complex environments – flooded forests and agricultural grasslands. Many of the forest flood mapping techniques rely on the contrast between flooded and unflooded areas in the image. By exploiting the presence of the double-bounce scattering mechanism characterizing the flooded forest areas, the contrast is increased. The double-bounce scattering mechanism can be represented by the HH–VV polarimetric channel. A study was carried out on the wetlands of Estonia to assess the increase of contrast between flooded and unflooded forest when using the HH–VV polarimetric channel rather then HH **[I]**. Deciduous and coniferous patches of forest with varying height were analyzed in respect to backscattering coefficients and polarimetric phase difference on high resolution TerraSAR-X images during flooding in the leaf-off season. An increase of difference between the backscatter of flooded and unflooded forest was reported for all height classes when using the HH–VV polarimetric channel, with the improvement over the HH channel ranging from 0.2 dB to 1.6 dB. Larger increase was recorded for deciduous cases as the leaf-off season allowed for a better canopy penetration increasing contribution from the trunk-ground interaction. Similarly, the increase was more pronounced for shorter tree patches.

Availability of high-resolution multi-polarization SAR data allows to investigate new techniques for characterizing the vegetation on agricultural grasslands and for detecting mowing events. A remote sensing campaign was organized in the summer of 2013 in Estonia covering 11 agricultural grasslands. During the campaign, an extensive field work campaign was carried out to complement X- and C-band acquisitions from TerraSAR-X, COSMO-SkyMed, and RADARSAT-2 over the course of the vegetative season. TerraSAR-X and RADARSAT-2 data were used to compute various PolSAR parameters, including the full H/A/α [96] and dual-pol H2α [97]

decompositions, and to compare them to the field survey data **[III]**. Two parameters were found to be related to mowing events – HH/VV polarimetric coherence and scattering entropy. Higher revisit times and shorter wavelength seemed to benefit the TerraSAR-X acquisitions as the relationship was more pronounced when compared to RADARSAT-2. The observations were also analyzed using a vegetation particle model, and the results indicate the potential use of these parameters for detecting mowing events.

COSMO-SkyMed data, on the other hand, were used to investigate the potential use of X-band one-day repeat-pass InSAR for monitoring of agricultural grasslands **[II,IV]**. Time series of four interferometric pairs were analyzed in relation to mowing events, and vegetation parameters. An increase of the interferometric coherence calculated for each interferometric pair was recorded after mowing events. However, precipitation and farming activity decreased the coherence rendering the detection impossible. The interferometric coherence was found to be inversely correlated to the vegetation height and wet above-ground biomass. The short wavelength of X-band, and one-day temporal baseline contribute to decorrelation at relatively low grass height levels. However, isolating the temporal coherence term, and limiting the grass height to an interval between 0 m and 1 m, very strong correlation was found between the height and the temporal coherence term, with a coefficient $r = 0.81$. Additionally, the temporal coherence was related to the height of vegetation on grasslands through random motion of scatterers in the vegetation layer.

2. FLOOD DETECTION

2.1. Polarimetric Effects in SAR signal over areas of flooded forest

Flooded forest is a composite environment where the scattering of the radar signal is governed by several mechanisms. A widely used approach [63, 98] describes the total backscattered signal σ^0 as consisting of the following parts:

- σ_c^0: scattering from the forest canopy
- σ_m^0: multi-path scattering between the canopy and the surface
- σ_t^0: scattering from the tree trunks
- σ_s^0: scattering from the surface
- σ_d^0: double-bounce scattering between the trunks and the surface

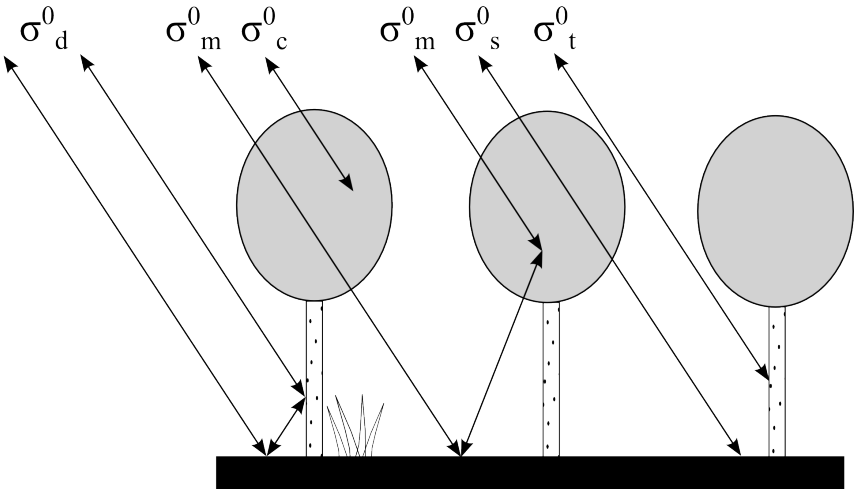

Figure 2.1: Scattering mechanisms of flooded forests (based on Townsend [98]).

These scattering mechanisms are illustrated in Figure 2.1. Water surface in the flooded forest acts as a specular reflector, while in the unflooded case the surface can be described as a Bragg surface [99], where the surface roughness causes diffuse reflection [100]. Thus, when flooding occurs, three mechanisms are affected: multi-path scattering increases, scattering from the surface decreases, and double-bounce

scattering increases [98]. The overall returned backscatter increases [60], giving rise to flood mapping techniques.

When analyzing the double-bounce scattering occurring in the case of a flooded forest, the upright tree trunk and the water surface act as a dihedral corner reflector made of two dielectric plane surfaces [101]. Scattering from the surfaces of the dihedral is described by the Fresnel's equations [102]. One prominent effect of the double-bounce scattering is the 180° phase difference between the HH and the VV polarized signals. If the orientation of the electromagnetic wave is normal to the plane of incidence (HH), the reflected wave differs in phase by 180° from the incident wave. However, if the orientation of the incident wave is in the plane of incidence (VV), no such phase shift occurs, see Figure 2.2. After the double reflection, the relative phase difference between the HH and the VV waves will be 180°.

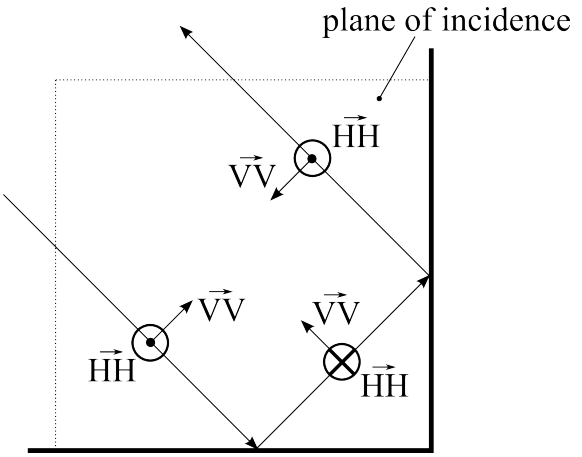

Figure 2.2: Phase changes in HH- and VV-polarized waves due to the double surface scattering at a dihedral.

If the surfaces of the dihedral are made out of an ideal conductor, the phase shift is 180° for all incidence angles θ_i. However, if the surfaces are dielectric (as in the case of natural targets), the phase shift depends on the incidence angle, with the maximum shift occurring at $\theta_i = 45°$ [100].

Other scattering mechanisms can introduce polarimetric effects as well [103]. The anisotropic nature of canopy can cause the HH and VV polarized signal to propagate through it with different speeds, causing a phase difference [104]. The phase difference for the surface and trunk scattering depends on the complex dielectric constant and the incidence angle, but is considered to be a minor contributor [104, 69].

2.2. The HH–VV polarimetric channel

The phase difference between the HH and VV signals can be expressed in terms of the actual difference in phase, or by using the notation of the HH–VV polarimetric channel. SAR is a coherent instrument, and the received data is often expressed in the complex form, i.e. $a + ib$, providing information about both the amplitude and the phase of the signal (pixel). This also allows for the implementation of composite polarimetric channels. One implementation is based on the 2×2 matrices form the Pauli matrices group, providing linear combinations of HH, VV, and HV channels: HH+VV, HH–VV, and HV [40]. Given the complex notation, the HH–VV channel will then be maximum when the HH and VV components are out of phase, and minimum when in phase. Thus, the HH–VV polarimetric channel can be used to evaluate the forest flooding in SAR images, and it might provide more contrast when compared to the HH channel.

2.3. The Soomaa experiment

To study the difference between the HH and the HH–VV backscatter from a flooded forest an experiment was carried out in the Soomaa National Park, Estonia. Forest patches with varying height and tree species were analyzed during flooding. The variability of patches would provide more information about the dependence of the HH/VV phase difference on tree species, and on the tree height.

Two acquisitions of the TerraSAR-X satellite were used in the study, representing unflooded and flooded conditions. The data were acquired during the ascending pass in the Stripmap HH/VV dual-pol Single Look Slant Range Complex mode with a swath width of 15 km, slant range resolution of 1.2 m, and azimuth resolution of 6.6 m, and an incidence angle of 23°. Data were calibrated to σ^0, ignoring the Noise Equivalent Beta Nought (NEBN) term.

A total of 12 forest patches were selected, and they were divided into two groups, see Table 2.1. The first group (F group) contained patches that were unflooded on March 3 but flooded on March 25, 2012. The second group contained patches that were unflooded on both occasions. The F group was used to analyze the change of HH and HH–VV backscatter due to flooding (F). The U group provided measurements for changes in backscatter and phase difference due to other factors. For a detailed map of the study area with the forest patches, please refer to Publication **I**, Figure 1.

Figure 2.3 provides an overview of the water level (relative to a long-term minimum) and air temperature in the period of acquisitions. The information was gathered at the Riisa hydrometric station ≈2 km from the study site [105]. Information about the water level allowed to simulate the flooded area using LiDAR measurements ac-

NR	Coniferous / Deciduous (%)	Tree height (m)	Cover (%)
CF1	86 / 14	23–28	80
DF1	0 / 100	20–28	75
CF2	70 / 30	16–18	75
DF2	5 / 95	14–19	81
CF3	80 / 20	7	77
DF3	0 / 100	5–7	78
CU1	91 / 9	25–29	71
DU1	0 / 100	23–24	73
CU2	87 / 13	12–16	75
DU2	38 / 62	14–16	67
CU3	90 / 10	1–10	76
DU3	3 / 97	5–10	77

Table 2.1: Parameters of the forest patches.

quired over the area in 2010 using the method outlined in Horritt *et al.* [103]. The LiDAR data were also used to determine the tree height for patches were inventory was done before 2010. Otherwise, data from Estonian National Forest Service [106] were used.

2.4. Results from the HH and HH–VV measurements

The set of images used for calculations is shown in Figure 2.4. An increase in the contrast between the acquisition dates is evident for HH and HH–VV channels. The flooded forest areas are clearly seen on the right side (Figure 2.4(b) and (d)) as the areas with higher backscatter.

An increase of σ^0 was recorded on both channels and for all F (flooded) patches (See Figure 2.5 for CF (coniferous-flooded) patches, and Figure 2.7 for DF (deciduous-flooded)). In general, the increase of σ^0 due to flooding was larger for smaller trees, i.e. the largest HH and HH–VV difference for coniferous patches was recorded for CF3 (height < 10 m) – 4.8 dB and 5.0 dB, respectively. Similarly, the largest differences of 8.2 dB and 9.8 dB were recorded for HH and HH–VV, respectively, over the DF3 patch.

In all the cases, a larger σ^0 increase due to flooding was recorded in the HH–VV channel rather than the HH channel. The difference was in the range from 0.2 dB (CF3) to 1.6 dB (DF3). Larger differences between HH σ^0 and HH–VV σ^0 were recorded for deciduous patches – on average, a difference of 0.77 dB (coniferous) vs. 1.3 dB (deciduous).

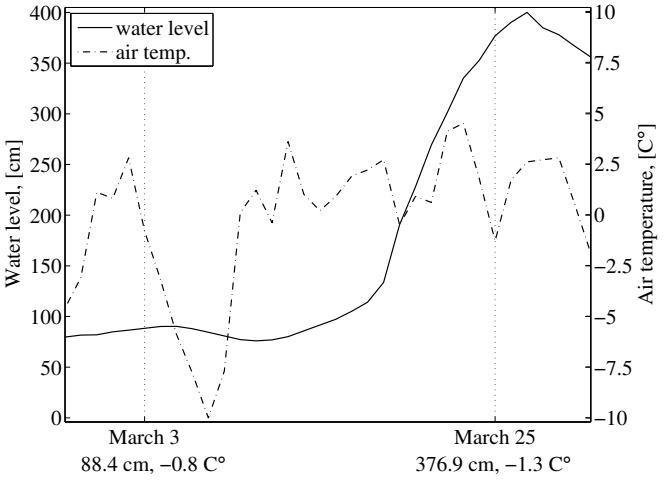

Figure 2.3: Water level (left y axis) and air temperature (right y axis) measured at the Riisa hydrometric station during the period of TerraSAR-X acquisitions. Acquisition dates (March 3 and March 25) are marked in the graph with a vertical dotted line, and the respective measurement values are given.

Results from the U (unflooded) patches (Figure 2.6 for coniferous, and Figure 2.8 for deciduous) indicate that the increase of backscatter for HH and HH–VV is due to the inundation. For the U patches, the changes of σ^0 between the acquisition dates are random, and not related to polarization or to recorded characteristics of the forest patches.

The aforementioned results suggest that, while the HH–VV provides larger contrast between the acquisition date, it is dependent on the amount of vegetation present in the patch. The σ^0 difference between the unflooded and the flooded cases for the HH–VV channel increased with decreasing tree height. Additionally, larger differences were recorded for deciduous patches. The study took place during the leaf-off season, and the deciduous patches had less foliage present than the coniferous patches.

In order to verify that the radar signal travels through the canopy and interacts with the surface under it, the relative phase difference between the HH and VV channels was measured. All F patches show a shift of phase difference values away from 0° for March 25 acquisition when compared to March 3. The effect is stronger for deciduous patches, with the mean phase shift more than doubled in the case of DF2 vs CF2 (23° vs 11°) and DF3 vs CF3 (28° vs 10°). For U patches, the recorded phase difference were in the range between 5° and 8°, indicating additional contributions

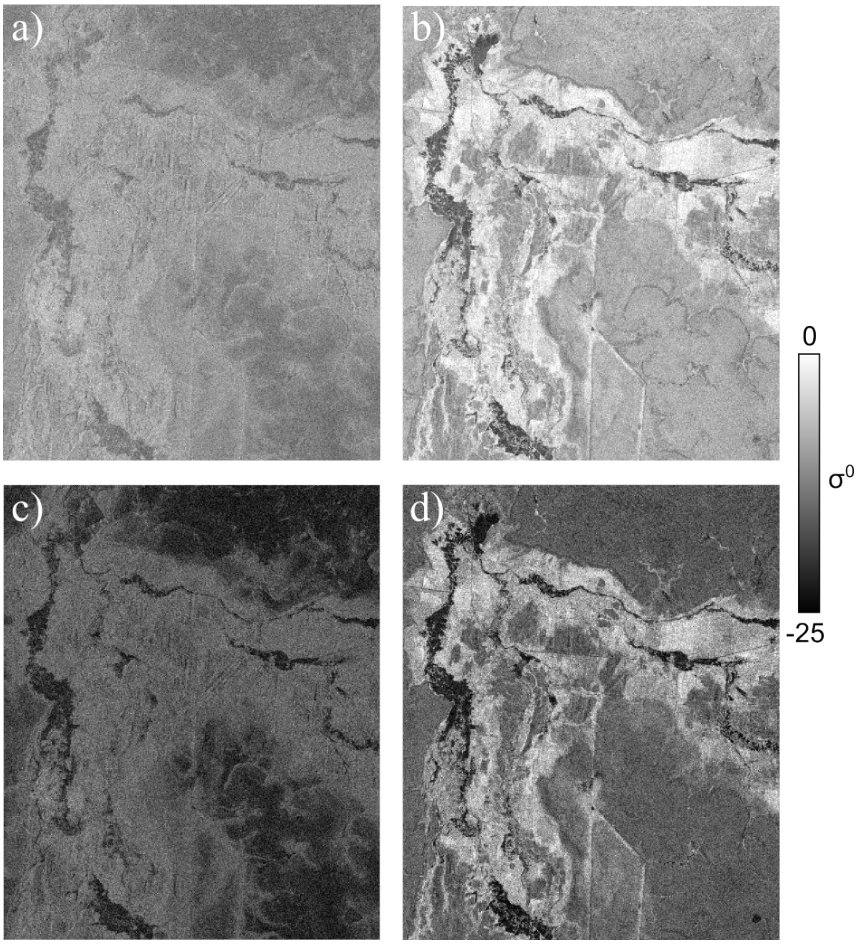

Figure 2.4: Intensity images of the acquisitions used in the study (calibrated to σ^0): HH on March 3 (a) and on March 25 (b), and HH–VV on March 3 (c) and on March 25 (d).

the phase shift effect from canopy and the surface. In order to evaluate the possible surface contribution, a patch of bare earth was analyzed on both acquisitions. The recorded increase of σ^0 between the dates was 5.5 dB and 5.0 dB for HH and HH–VV, respectively. The phase shift effect, on the other hand, was very small with the difference recorded at 1° (from 40° to 41°).

The recorded phase difference values for F patches are relatively small in relation to 180° in case of a perfectly conducting dihedral. This is partially explained by the

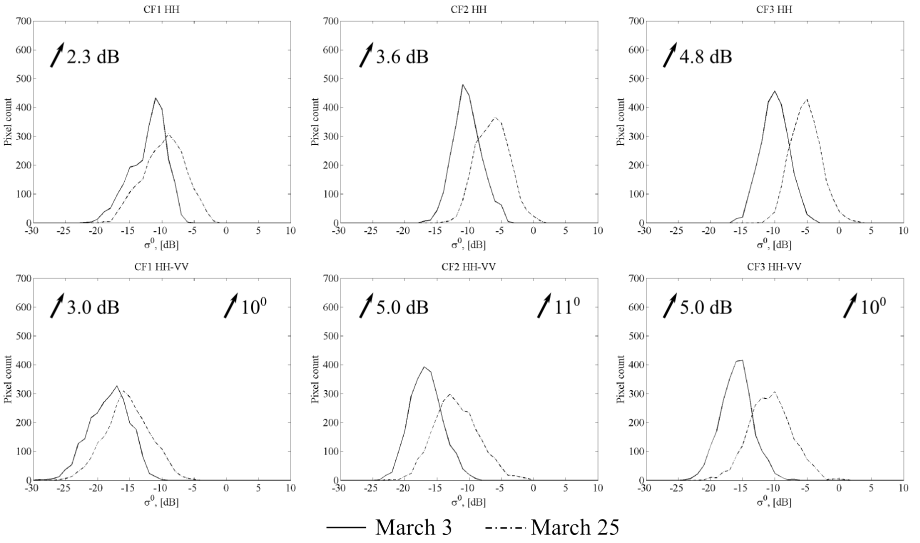

Figure 2.5: Distributions of σ^0 values for CF patches on March 3 (solid line) and March 25 (dotted line). Top row – HH channel, bottom row – HH–VV channel. Changes of the mean σ^0 and phase shift values between the acquisition dates are given on the graphs.

steep incidence angle (23°) as for a dihedral with dielectric surfaces the maximum phase shift occurs at 45° (see Section 2.1.). The general trend that larger double-bounce effects are recorded for deciduous patches and for patches with lower tree height suggest a strong attenuation of the X-band signal in the canopy, reducing the amount of signal that would reach the surface under the canopy and exhibit the phase shift characteristic to the dihedral.

2.5. Summary of the study

Study confirmed that the HH–VV polarimetric channel provides larger separation between flooded and unflooded forest areas than the HH channel. However, the gain of using the HH–VV channel (i.e. difference between HH–VV and HH) is small, ranging from 0.2 dB to 1.6 dB. This is most likely attributed to the steep incidence angle (23°) and canopy attenuation due to the short wavelength of the X-band (≈3 cm). The attenuation effect was evident as larger separation was achieved for deciduous patches due to the leaf-off season. Furthermore, the increase of σ^0 values due to flooding was larger as the tree height decreased.

Overall, in the given environment employing the presence of the double-bounce

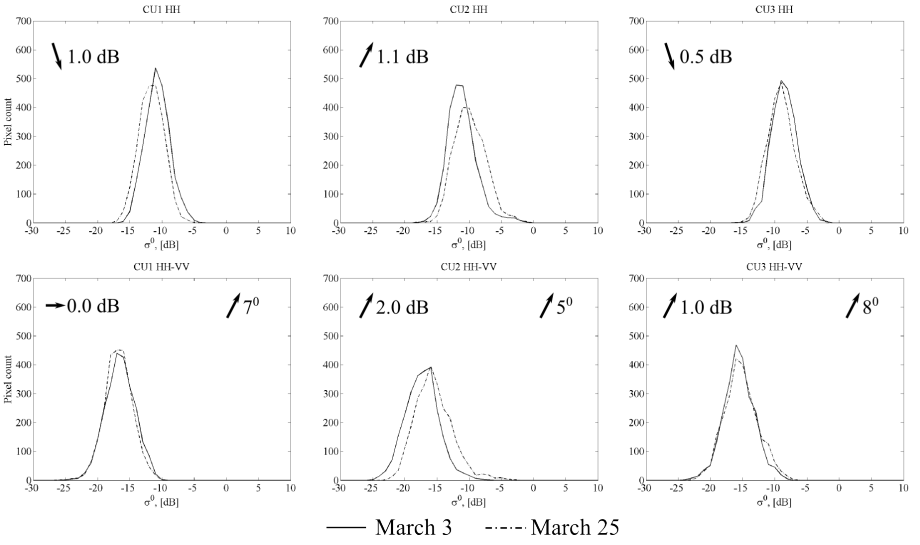

Figure 2.6: Distributions of σ^0 values for CU patches on March 3 (solid line) and March 25 (dotted line).

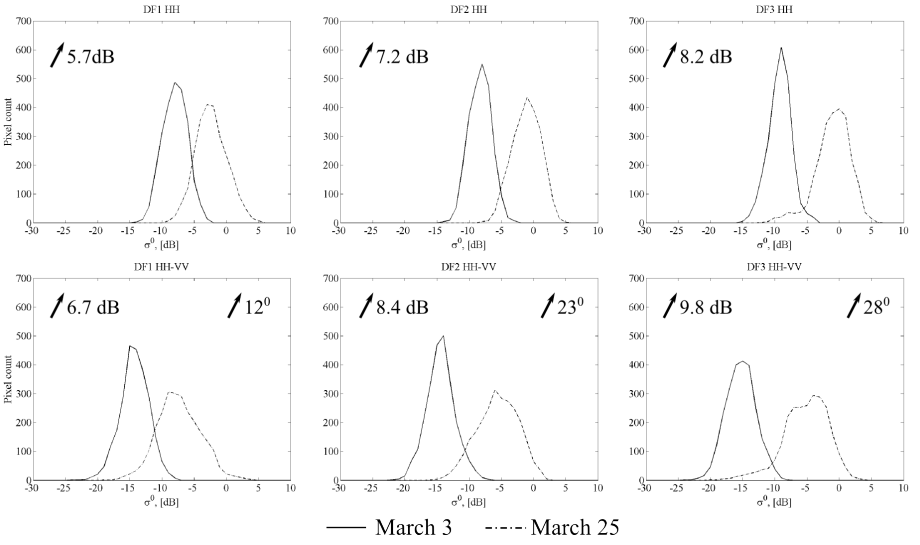

Figure 2.7: Distributions of σ^0 values for DF patches on March 3 (solid line) and March 25 (dotted line).

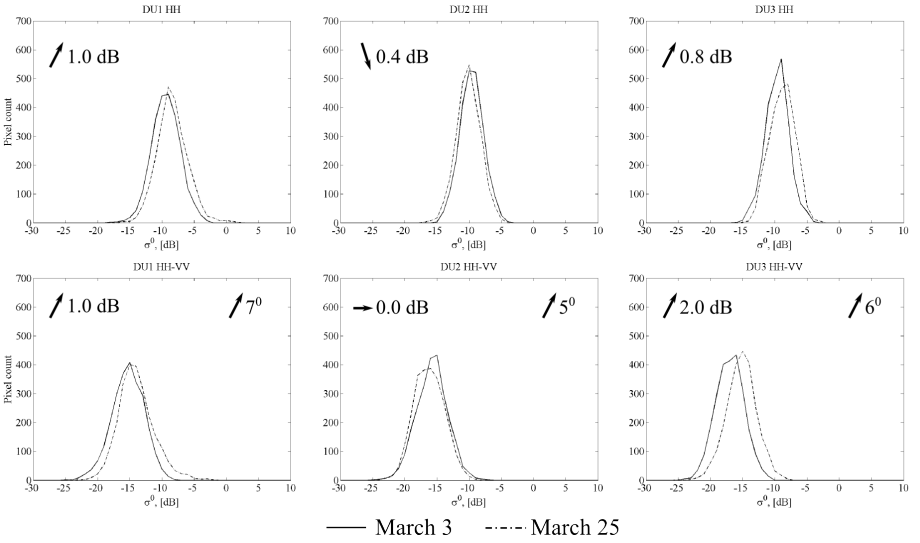

Figure 2.8: Distributions of σ^0 values for DU patches on March 3 (solid line) and March 25 (dotted line).

scattering mechanism by using the HH–VV polarimetric channel provides increased separation between flooded and unflooded forest areas when compared to using the HH channel. However, the increase is relatively small, and shallower incidence angles (close to $45°$) and longer wavelengths should be considered in similar future studies. Alternatively, the phase shift information itself might be used as a thresholding parameter to delineate flooded and unflooded forests. For all flooded patches, the phase shift was larger than $10°$. For the unflooded patches, on the other hand, the phase shift was smaller than $10°$.

3. MONITORING OF GRASSLANDS

3.1. Polarimetric and Interferometric Effects of Short Vegetation

3.1.1. Detection and evaluation of polarimetric scattering from the grassland canopy

Grasslands constitute a composite environment where several backscattering mechanisms can occur, see Figure 3.1 [107]. The main mechanisms involved in backscattering from grasslands are:

- σ_m^0: multi-path scattering between the canopy and the surface
- σ_d^0: double-bounce scattering between the canopy and the surface
- σ_c^0: scattering from the grass canopy
- σ_s^0: scattering from the surface

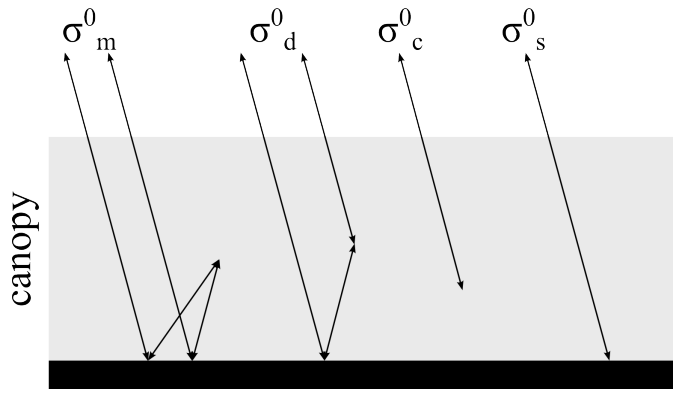

Figure 3.1: Scattering mechanisms of grasslands. Based on Toure *et al.* [107]

Apart from the mechanisms mentioned in Figure 3.1, additional scattering mechanisms can occur due to the presence of thatch layer and volume scattering from the soil. A layer of thatch can contribute several backscattering terms when wet [108]. Additionally, dry soil can contribute volume scattering, especially at shorter wavelengths [109]. The aforementioned effects should be considered in cases when the grassland vegetation is not present.

The relative power of the individual mechanisms mentioned in Figure 3.1 is dependent on characteristics of the vegetation [110, 111], as well as on wavelength, polarization, and incidence angle (satellite parameters) [100]. For a fixed case of satellite parameters, changes in the backscatter can be associated to changes in vegetation. In this thesis, the following polarimetric variables are analyzed in relation to changes in the grasslands vegetation: HH/VV ratio, HH/VV coherence phase and magnitude, T_{12} coherence magnitude, HV σ^0, and parameters from the quad-pol H/A/α [96] and dual-pol H2α [97] decompositions.

The HH/VV parameters are based on the anisotropic nature of grassland vegetation. Most of the above ground biomass is contained in stalks [112], and they interact strongly with the VV polarized signal [40]. On the other hand, when the vegetation is cut and part of it left on the ground for collection, the horizontally oriented vegetation interacts with the HH signal. Thus, analysis of the dynamics of the HH and VV polarized backscatter can provide information about the orientation of the observed vegetation. The HH/VV ratio ($ratio_{hhvv}$), and the HH/VV coherence (γ_{hhvv}) can be calculated as follows:

$$ratio_{hhvv} = \frac{|\langle S_{HH} \rangle|^2}{|\langle S_{VV} \rangle|^2} \tag{3.1}$$

$$\gamma_{hhvv} = \frac{\langle S_{HH} \cdot S_{VV}^* \rangle}{\sqrt{\langle |S_{HH}|^2 \rangle \cdot \langle |S_{VV}|^2 \rangle}} \tag{3.2}$$

where S_{XX} denotes recorded backscatter of polarization XX, $\langle\rangle$ denotes ensemble average, * denotes the complex conjugate, and $||$ mark the absolute value.

The T_{12} coherence magnitude $|\gamma_{T_{12}}|$ is calculated as:

$$\gamma_{T_{12}} = \frac{\langle (S_{HH} + S_{VV}) \cdot (S_{HH} - S_{VV})^* \rangle}{\sqrt{\langle |S_{HH} + S_{VV}|^2 \rangle \cdot \langle |S_{HH} - S_{VV}|^2 \rangle}} \tag{3.3}$$

The $|\gamma_{T_{12}}|$ parameter analyzes the correlation of two linear combinations, $S_{HH} + S_{VV}$ and $S_{HH} - S_{VV}$, that are strongest in case of surface and double-bounce scattering, respectively.

The HV σ^0 indicates the power of volume scattering, i.e. σ_c^0. The HV term is widely used to analyze vegetation as the anisotropic nature of vegetation targets (differently oriented features such as branches and leaves) causes the change of signal polarization.

The quad-pol H/A/α [96] and dual-pol H2α [97] decompositions use eigenvector analysis of the coherency matrix $\boldsymbol{T}_3$ (or $\boldsymbol{T}_2$ in case of the dual-pol data). The parameters provided by the decompositions are [40]:

- **Entropy H.** Indicates the randomness or the depolarizing power of the scatterer. Low values of H (closer to zero) describe weakly depolarizing systems with a recoverable dominant scattering mechanism, while values close to one indicate a depolarizing system with a mix of scattering mechanisms.
- **Anisotropy A.** A complementary parameter to H, the A indicates the relative power of the second and the third strongest scattering mechanisms.
- **Dominant (α) and mean ($\bar{\alpha}$) scattering alpha angle.** The α parameter indicates the dominant or the mean scattering mechanism, and the values of the parameter range from 0° (surface scattering) to 45° (volume scattering) to 90° (double-bounce scattering).

From the point of view of short vegetation, the aforementioned decomposition parameters may provide information about the vegetation structure and characteristics. Voormansik *et al.* [91] reported a significant change in the dual-pol (HH/VV) α, $\bar{\alpha}$, and γ_{hhvv} parameters after a mowing event in the case when some vegetation was left on the ground. However, the study used a limited data set with dual-pol single frequency, and fixed incidence and orientation angles. Additionally, the field survey was mainly qualitative. By improving the field survey and expanding the data set, a more definite relation could be established between the PolSAR parameters and the characteristics of short vegetation.

3.1.2. SAR interferometry of grasslands: evaluation of the temporal coherence term

SAR interferometry aims to exploit the complex correlation coefficient calculated from two complex images [20, 113]:

$$\gamma = \frac{\langle s_1 s_2^* \rangle}{\sqrt{\langle s_1 s_1^* \rangle \langle s_2 s_2^* \rangle}} \tag{3.4}$$

where s_1 and s_2 denote values from the two complex co-registered images, $\langle\rangle$ denotes ensemble average, and * denotes the complex conjugate. The coefficient's phase is the expected interferometric phase, and its magnitude is related to phase noise [20]. The parameter can be expressed as a product of several contributions [114, 115]:

$$\gamma_{total} = \gamma_v \gamma_t \gamma_{SNR} \gamma_{bias} \tag{3.5}$$

All terms in Eq. 3.5 are normalized to the range between 0 and 1, with the value 1 indicating no decorrelation and maximum coherence. The constituents of Eq. 3.5 can be written out as follows:

- γ_v: volume coherence, measuring decorrelation due to the presence of a volume, e.g. forest or other vegetation. Resolution of this phenomena is dependent on spatial baseline, i.e. physical distance between the two acquisition platforms. Increasing the baseline increases the resolution but decreases the γ_v
- γ_t: temporal coherence, measuring decorrelation due to changes (e.g. movement) in the resolution cell over the temporal baseline
- γ_{SNR}: measures system noise
- γ_{bias}: accounts for the bias in estimating the coherence [116]

In this study, use of temporal coherence γ_t for detecting mowing events and characterizing the grassland vegetation is evaluated. Therefore, contribution from γ_t must be isolated from the other terms. The γ_{SNR} can be evaluated from the signal-to-noise ratio (SNR) [115, 117]:

$$\gamma_{SNR} = \frac{1}{1 + SNR^{-1}} \tag{3.6}$$

where the SNR is the ratio between the observed σ^0 and the noise equivalent sigma zero (NESZ) [118]. The γ_{bias} term is dependent on the number of samples used when calculating the coherence [119]. Larger number of samples decreases the bias decorrelation, increasing the γ_{bias} towards the value 1.

Contribution from γ_v can be evaluated by analyzing the vertical wavenumber κ_z [120]:

$$\kappa_z = \frac{2\pi}{h_a} \tag{3.7}$$

where h_a is the height of ambiguity that itself is calculated as follows [120]:

$$h_a = \frac{\lambda R \sin\theta}{2B_n} \tag{3.8}$$

where λ is the wavelength, R – range to the target, θ – incidence angle, and B_n – perpendicular baseline.

Having evaluated the other decorrelation terms, γ_t may be expressed from the γ_{total}. The γ_t itself is the measure of physical change in the resolution cell over the time defined by the temporal baseline. The changes may be caused, for example, by movement of the objects or by change in the dielectric constant. Changes in the vegetation layer may cause decorrelation of the correlation coefficient, and these changes may be evaluated through the γ_t term.

3.1.3. Polarimetric and interferometric effects due to mowing and changes in grassland vegetation

Physical changes in the grassland vegetation, such as mowing or growing, cause changes in the radar backscatter as well. It stems from the fact that the radar signal is inherently sensitive to the orientation, structure and water content of the vegetation [40]. The actual changes in the backscatter, however, depend on (in addition to changes the vegetation) acquisition parameters, such as the wavelength and the incidence angle.

In [91], Voormansik *et al.* reported a limited success relating dual-pol PolSAR parameters to mowing events. However, attempts to relate certain PolSAR parameters to grass height were unsuccessful. On the other hand, sensitivity of γ_t to vegetation height in the case of farmlands is reported in [84, 121, 95]. These studies used C-band (wavelength of ≈5 cm) and one-day or larger temporal baselines. The observed coherence values decreased as the crop height increased. The phenomena was explained by the soil cover fraction, i.e. growing vegetation screening the soil thus decreasing the coherent contribution from it and increasing contribution from the highly decorrelating vegetation. The decorrelating effect of the vegetation can be attributed to its motion. Zebker and Villasenor [115] expressed the γ_t term as a function of the root mean square (RMS) motion of scatterers in the resolution cell σ_{rms}, wavelength λ, and temporal baseline t:

$$\gamma_t = e^{-\frac{t}{\tau}}, \tau = \frac{2}{\sigma_{rms}^2}\left(\frac{\lambda}{4\pi}\right)^2 \tag{3.9}$$

The exact relation of vegetation height to σ_{rms}, and to γ_t, however, is unknown and is dependent on many biophysical parameters and weather effects.

On the other hand, mowing is a very profound change in the vegetation structure. This change, as reported earlier in [91], can be detected with PolSAR as the removal of the vegetation layer causes changes in the polarimetric radar returns. The changes, however, are detectable if some of the vegetation is left lying on the field after cutting. In the case of InSAR, removal of vegetation exposes the soil underneath, increasing the temporal coherence. Care must be taken in regard to precipitation and farming activities that might take place between the repeat-pass acquisitions, as changes caused by these effects may decrease the coherence drastically [84].

3.2. Measurement Campaign

In order to evaluate the use of InSAR and PolSAR parameters for detection of mowing events and characterizing grassland vegetation, a measurement campaign was

undertaken during the summer of 2013. Eleven agricultural grasslands in Central Estonia were selected for an extensive field survey campaign, see Figure 3.2. The area is predominantly covered by agricultural fields and occasional forest patches. The relief is relatively flat, with the elevation ranging from 40 m in the west to 85 m in the east [122]. The selected fields are used mainly for hay production, and owners claiming subsidy support are obliged to adhere to specific management practices, including mowing. The fields are of different sizes, and during the summer of 2013 they were used to grow a variety of plant species. For an overview of the test fields, please refer to Table 3.1.

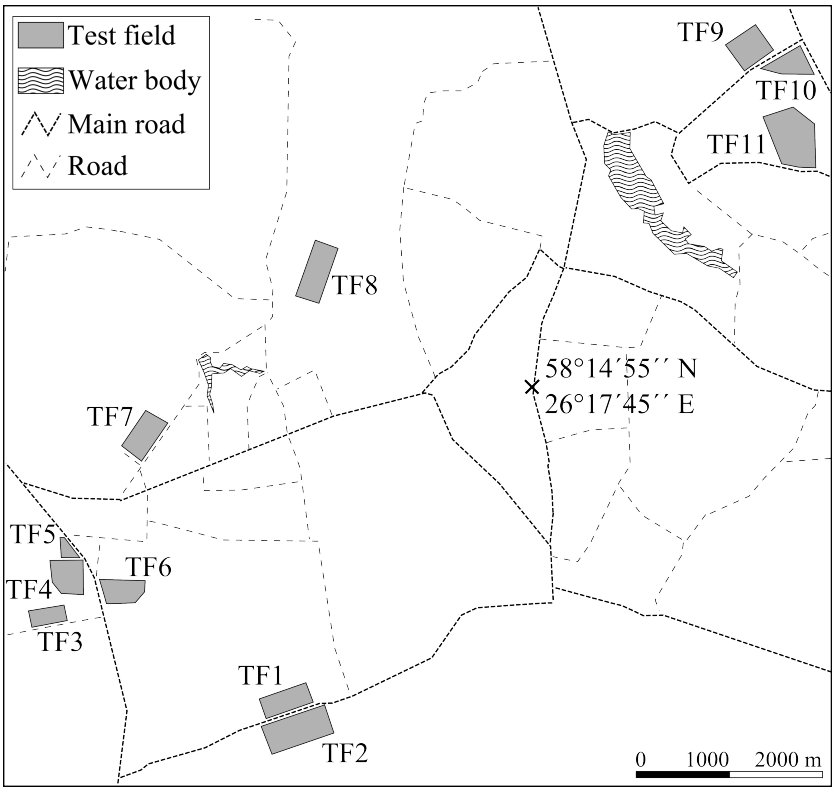

Figure 3.2: Rannu test site with the test fields marked on the map.

Field surveys took place from May 11 until October 5 and they were carried out simultaneously with the SAR acquisitions. During the surveys, a 0.5×0.5 m^2 frame was placed on the ground and the height of the vegetation inside it was measured. The vegetation was then cut and weighed. Afterwards, the collected samples were dried to a constant weight and the dry weight was recorded. Additionally, soil moisture of

Field Nr.	Area [ha]	Primary species	min/max height, [m]	min/max wet biomass, [kg/m^2]
TF1	13.0	Taraxacum officinale Trifolium pratense	0.10 / 0.70	0.24 / 2.9
TF2	24.9	Trifolium pratense Elymus repens Artemisia vulgaris	0.10 / 0.80	0.20 / 3.4
TF3	4.8	Trifolium pratense Galium aparine Artemisia vulgaris	0.0 / 0.60	0.0 / 3.5
TF4	9.3	Dactylis glomerata Alopecurus pratensis	0.10 / 1.2	0.24 / 2.5
TF5	4.0	Phalaris arundinacea	0.0 / 1.8	0.0 / 4.7
TF6	9.1	Elymus repens	0.05 / 1.0	0.09 / 4.4
TF7	11.3	Trifolium pratense Taraxacum officinale Artemisia vulgaris Elymus repens Matricaria perforata	0.0 / 0.60	0.0 / 3.5
TF8	12.3	Trifolium pratense Elymus repens Matricaria perforata	0.05 / 0.70	0.19 / 3.4
TF9	10.1	Trifolium pratense Rumex sp. Matricaria perforata	0.10 / 0.70	0.16 / 5.2
TF10	10.9	Festuca rubra Phalaris arundinacea Capsella bursa-pastoris	0.07 / 0.80	0.22 / 3.5
TF11	12.6	Trifolium pratense Alopecurus pratensis Poa sp. Taraxacum officinale Artemisia vulgaris	0.03 / 0.75	0.40 / 7.3

Table 3.1: Size, primary species, and minimum and maximum recorded values of height and wet above round biomass for the test fields used in the study.

the upper 5 cm layer was recorded using two hand held conductivity probes (Delta-T ML2x and Extech MO750). The soil moisture measurements were calibrated for comparability. Photos of the test fields were also taken to provide reference about the conditions on the fields.

As the plant species present and conditions on the grasslands varied from field to field, the recorded height and biomass measurements during the campaign vary as well, see Table 3.1. Majority of the fields were used for growing red clover (*Trifolium pratense*), the common dandelion (*Taraxacum officinale*), and common mugwort (*Artemisia vulgaris*). The vegetation on these fields was allowed to reach the height of ≈0.8 m before mowing, and the maximum wet above ground biomass weighed at around 3.0 kg/m^2. The exceptions were TF9 and TF11, were the density of the plants was greater and the weight exceeded 5.0 kg/m^2. TF4, TF5, and TF6 were used for growing different grass species, and in the case of TF5 the maximum height was recorded at 1.8 m. The dominant species on TF10 was red fescue (*Festuca rubra*).

In total, acquisitions from three SAR instruments were scheduled – TanDEM-X (TDX), RADARSAT-2 (R2), and COSMO-SkyMed (CSK), see Table 3.2. TDX and R2 acquisitions were used for the PolSAR calculations. CSK images were used for InSAR, and they were organized into four two-image pairs with one-day temporal baseline. The spatial baseline, height of ambiguity, and κ_z (see Section 3.1.2.) for the CSK pairs are given in Table 3.3.

Table 3.4 summarizes the PolSAR and InSAR parameters calculated from the SAR data (see Sections 3.1.1. and 3.1.2.). For the TDX dataset, HV channel was estimated according to [123]. Processing was performed in Next ESA SAR Toolbox, Matlab, and IDL. The TDX data was smoothed by a 18 $\times$ 10 window in range and azimuth, respectively, yielding equivalent number of looks (ENL) of 113 (ascending pass) and 118 (descending pass). R2 data was smoothed by a 9 $\times$ 13 (range and azimuth) window yielding ENL 67. The CSK images in each pair were co-registered to sub-pixel accuracy, and the interferometric coherence was computed using a 7 $\times$ 7 window. No reprojection was performed on the SAR data. For all datasets, the σ^0 values were calculated using calibration constants provided in the accompanying meta-data files.

Data were also collected about weather conditions in the study area during the SAR acquisitions. The Tõravere meteorological station 7–16 km to the East of the study area provided information about the air temperature and precipitation amount [105].

	TanDEM-X asc. pass	TanDEM-X desc. pass	RADARSAT-2	COSMO-SkyMed
Dates	19.04, 11.05, 22.05, 2.06, 13.06, 24.06, 5.07, 16.07, 27.07	4.06, 15.06, 26.06, 29.07, 22.09	14.05, 7.06, 1.07, 25.07, 18.08, 11.09	1.06, 2.06, 17.06, 18.06, 19.07, 20.07, 20.08, 21.08
Data take start (UTC)	15:53	4:32	7:27	3:49
Mode	bistatic dual-pol spotlight	bistatic dual-pol spotlight	Fine Quad-Pol (FQ24)	Stripmap HIMAGE
Polari-zation	HH/VV	HH/VV	HH/HV/VH/VV	HH
Mean incidence angle	40.0°	44.5°	43.5°	37.0°
Resol., az. x gr. range (m)	3.20 x 1.84	3.20 x 1.68	7.60 x 7.55	3.00 x 3.00
Pixel spacing, az. x gr. range (m)	2.61 x 1.42	2.70 x 1.30	4.80 x 6.87	3.00 x 3.00

Table 3.2: Properties of the SAR acquisitions.

Pair	spatial baseline, [m]	h_a, [m]	κ_z, [rad/m]
Jun 1/2	203	29	0.22
Jun 17/18	190	30	0.21
Jul 19/20	128	45	0.14
Aug 20/21	112	52	0.12

Table 3.3: Properties of the CSK InSAR pairs.

3.3. Evaluation of the Vegetation Height

Correlation analysis was performed to establish a relation between the computed Pol-SAR and InSAR parameters, and the vegetation height and biomass. No significant

Instrument	Parameters used in the study
TDX	H2α (H, α), $ratio_{HHVV}$, γ_{hhvv} (phase and magnitude), $\lvert\gamma_{T_{12}}\rvert$, σ^0_{HV}
R2	HAα (H, A, α), $ratio_{HHVV}$, γ_{hhvv} (phase and magnitude), $\lvert\gamma_{T_{12}}\rvert$, σ^0_{HV}
CSK	$\lvert\gamma\rvert$, σ^0_{HH}

Table 3.4: Summary of the InSAR and PolSAR parameters used in the study.

correlation was established in the case of PolSAR parameters. The magnitude of the total interferometric coherence, $|\gamma_{total}|$, on the other hand, was found to be inversely correlated to vegetation parameters measured during the field surveys – height, wet above ground biomass, and dry above ground biomass, see Figure 3.3. Figure 3.3 presents the interferometric coherence calculated from the June 17/18 pair, and the actual height of vegetation and the $|\gamma_{total}|$ value is provided for a selection of test fields. The full time series of $|\gamma_{total}|$ in respect to vegetation parameters are presented in Publication **II**, Figure 3, and values for vegetation parameters, $|\gamma_{total}|$, and σ^0 are given in Publication **II**, Tables III and IV. In general, $|\gamma_{total}|$ decreased as the vegetation height increased. Additionally, decrease of $|\gamma_{total}|$ was caused by precipitation. Precipitation on July 19 caused decorrelation of $|\gamma_{total}|$ in the case of TF4 but not for TF9, TF10, and TF11 that had similar height values to TF4. TF4, however, had lower wet above ground biomass values and lower soil cover fraction. Thus, the soil was visible more in the case of TF4, causing lower $|\gamma_{total}|$ values for July 19/20 due to change in soil moisture.

To investigate further the relationship between $|\gamma_{total}|$ and vegetation parameters, temporal coherence $|\gamma_t|$ values were calculated (see Eq. 3.5). Given the CSK acquisition parameters, γ_t was believed to be the dominant contributor to γ_{total}. The spatial baseline, and the dependent κ_z values (see Table 3.3), when compared to the average vegetation height, indicate that the volume component γ_v contributed insignificantly. The other contributions (γ_{SNR} and γ_{bias}) were corrected for according to Section 3.1.2..

The calculated $|\gamma_t|$ are plotted versus the recorded vegetation height in Figure 3.4. An inverse correlation between the parameters is observed. A similar relationship exists in the case of wet above ground biomass, please refer to Publication **II**, Figure 4a. As reported by previous studies, $|\gamma_t|$ decreases with increasing vegetation height [95]. However, due to the relatively long temporal baseline (one day) and short wavelength (X-band, $\approx$3 cm), the decorrelation effect is severe. As seen in Figure 3.4, $|\gamma_t|$ values higher than 0.5 are observed only in the case of lack of vegetation. Vegetation height and photos describing the conditions are given in Figure 3.4. When the height

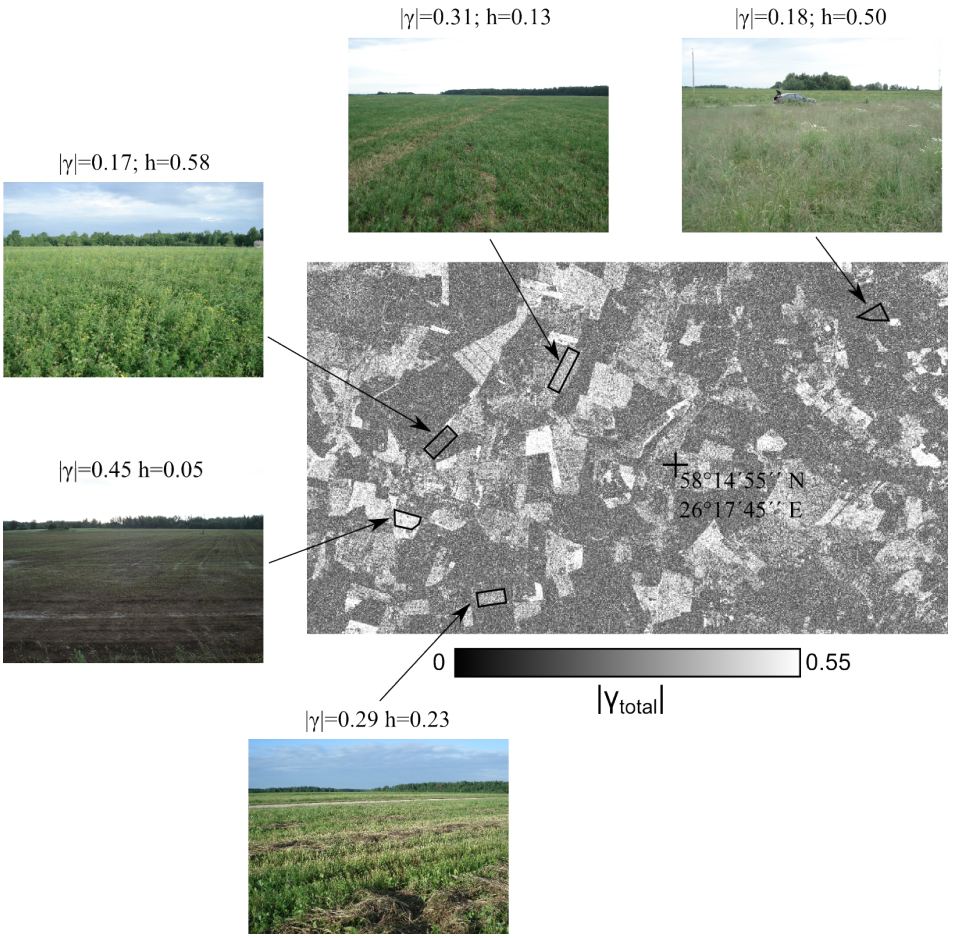

Figure 3.3: Coherence image of the study site from the June 17/18 CSK pair. Photos, $|\gamma_{total}|$, and height values given for some of the test fields.

reaches ≈0.1 m, the $|\gamma_t|$ values are halved to ≈0.4. At the height value of ≈0.25 m, total decorrelation occurs, i.e. larger height values correspond to similar $|\gamma_t|$ values (≈0.1).

$|\gamma_t|$ is significantly correlated to vegetation height ($r = -0.52$), wet above ground biomass ($r = -0.59$), and dry above ground biomass ($r = -0.53$). From Figure 3.4, the relationship seems logarithmic. After log-transformation, the correlation coefficients between $|\gamma_t|$ and the biophysical parameters are -0.63 (height), -0.70 (wet biomass), and -0.63 (dry biomass). To analyze further the relationship between $|\gamma_t|$ and short vegetation, the data set was limited to samples with height h_v

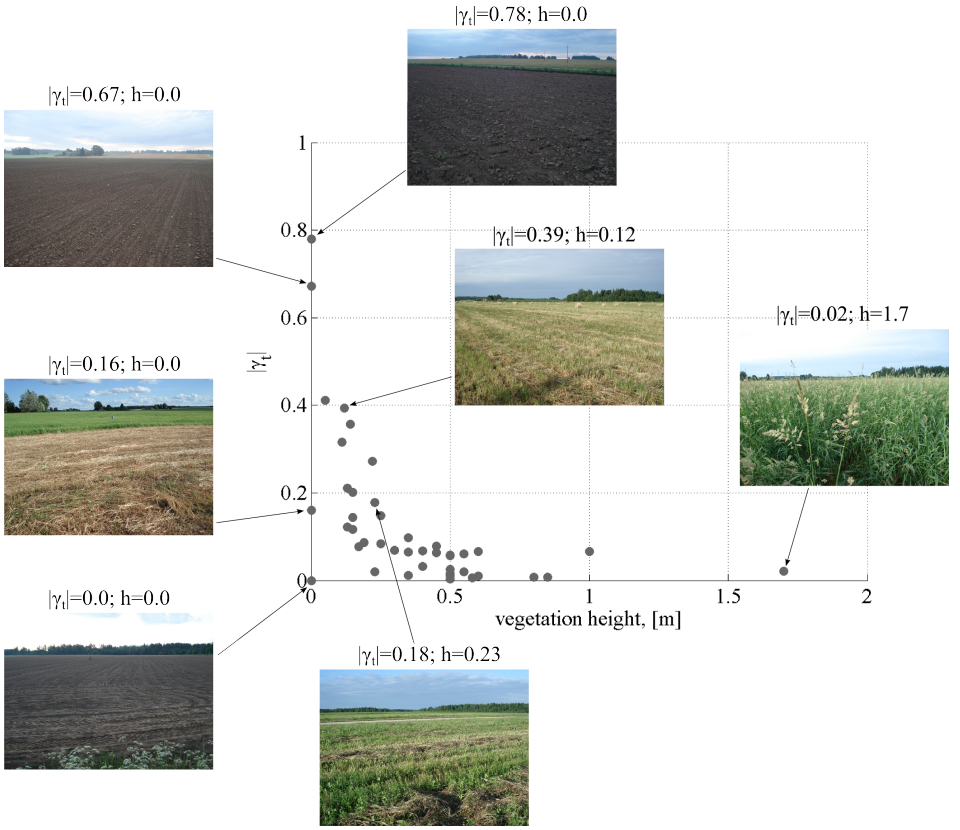

Figure 3.4: Scatter plot of vegetation height (x axis) vs $|\gamma_t|$ (y axis). Photos, $|\gamma_t|$, and height values given for some of the data points.

limited to a range $0 < h_v < 1$ m. The correlation coefficients for the limited data set $|\gamma_t^*|$ are -0.71 (height), -0.69 (wet biomass), and -0.60 (dry biomass). After the log-transformation, the coefficients are are -0.78 (height), -0.70 (wet biomass), and -0.58 (dry biomass). The results indicate the possibility to relate the $|\gamma_t|$ calculated from interferometric pairs of X-band acquisitions with one-day temporal baseline to height, wet biomass, and dry biomass of short vegetation over grasslands. While the relationship is statistically significant, further studies on the topic should investigate shorter temporal baselines and longer wavelengths. Publication **II**, Table VI gives further details about the correlation coefficients computed during the study.

The apparent logarithmic nature of the relationship between $|\gamma_t|$ and the vegetation height is similar to that mentioned in Section 3.1.2., i.e. relationship between $|\gamma_t|$ and the motion of scatterers σ_{rms} Eq. 3.9. By assuming that the decorrelation is

caused by the motion of scatterers in the resolution cell, Eq. 3.9 can be linearized:

$$|\log \gamma_t|^{0.5} = k\sigma_{rms} \tag{3.10}$$

where k summarizes the constant terms from Eq. 3.9. Assuming a linear relation between h_v and σ_{rms}, a similar linearization can be applied to $|\gamma_t|$ and h_v as well. After linearization the correlation coefficients for $|\gamma_t|$ are 0.63 (h_v), 0.71 (wet biomass), and 0.64 (dry biomass). For $|\gamma_t^*|$ (reduced data set), the coefficients are: 0.81 (h_v), 0.75 (wet biomass), and 0.63 (dry biomass).

3.4. Detection of Mowing Events

Detection of mowing events can be analyzed using both the InSAR and PolSAR techniques. Four mowing events coincided with the InSAR acquisitions: TP6 on June 1/2, TP5 on July 19/20, and TP3 and TP7 on August 20/21. Photos describing the conditions on the fields and $|\gamma_t|$ values are presented on Figure 3.4. In two cases the $|\gamma_t|$ values are relatively high, i.e. 0.67 for TP3 and 0.78 for TP7 – the highest recorded in the study. As discussed earlier, the high coherence values can be explained with backscattering from bare soil not inhibited by vegetation. However, precipitation during the acquisition of one of the InSAR images for TP5 introduced decorrelation due to a change in soil moisture, and $|\gamma_t|$ reduced to 0.16. Similarly, the low $|\gamma_t|$ value for TP6 (0.0) could be explained after examining the field survey photos. Between the InSAR acquisitions, the field was ploughed and fertilized, changing both the soil moisture and surface roughness. Thus, application of one-day repeat-pass X-band InSAR is limited due to sensitivity of the method to any changes during the temporal baseline, including precipitation and farming activities.

In the case of PolSAR, the time series of acquisitions were more dense than for InSAR, and the data could be analyzed in respect to more mowing events. Changes in parameters mentioned in Table 3.4 in respect to mowing events are summarized in Publication **III**, Table II (TDX) and Table III (R2). Two parameters stood out and showed the most consistent behavior – $|\gamma_{hhvv}|$ and H, see an overview in Table 3.5 (TDX evening passes – TDX/E), Table 3.6 (TDX morning passes – TDX/M), and Table 3.7 (R2).

For the majority of mowing cases, the $|\gamma_{hhvv}|$ decreased and H increased after the mowing. Out of 13 mowing events in the TDX/E series, this behavior was recorded for 11 cases. For TDX/M series, it was true for 4 out of 4 cases. For R2 series, the increase of H and decrease of $|\gamma_{hhvv}|$ was recorded for 10 cases out of 12 mowing events. From the point of view of magnitude of the changes, it was stronger for both TDX series and lower for R2. The R2 series had worse temporal coverage, i.e. the

	TF1 0–6	TF2 0–6	TF3 0–1	TF4/1 0–6	TF4/2 8–10	TF5/1 0–1	TF5/2 0–9
H	$\uparrow 0.21$	$\uparrow 0.067$	$\uparrow 0.025$	$\uparrow 0.14$	$\uparrow 0.079$	$\uparrow 0.042$	$\downarrow 0.039$
$\lvert\gamma_{hhvv}\rvert$	$\downarrow 0.27$	$\downarrow 0.071$	$\downarrow 0.048$	$\downarrow 0.27$	$\downarrow 0.12$	$\downarrow 0.069$	$\uparrow 0.015$
	TF6 8–10	TF7 3–4	TF8/1 7–8	TF8/2 0–9	TF9 0–9	TF10 0–9	
H	$\downarrow 0.021$	$\uparrow 0.042$	$\uparrow 0.15$	$\uparrow 0.023$	$\uparrow 0.043$	$\uparrow 0.00099$	
$\lvert\gamma_{hhvv}\rvert$	$\uparrow 0.034$	$\downarrow 0.073$	$\downarrow 0.23$	$\downarrow 0.049$	$\downarrow 0.081$	$\downarrow 0.00012$	

Table 3.5: Changes in H and $|\gamma_{hhvv}|$ parameters calculated from TDX/E data set related to mowing events. Each column corresponds to a mowing event, and the test field where the event occurred is given together with the possible time in days between the event and the 2nd acquisition. Values in the cells indicate the difference between the first acquisition prior to mowing and second acquisition after the event.

	TF1 2–8	TF2 2–8	TF4 2–8	TF8 9–10
H	$\uparrow 0.18$	$\uparrow 0.095$	$\uparrow 0.074$	$\uparrow 0.089$
$\lvert\gamma_{hhvv}\rvert$	$\downarrow 0.24$	$\downarrow 0.15$	$\downarrow 0.17$	$\downarrow 0.16$

Table 3.6: Changes in H and $|\gamma_{hhvv}|$ parameters calculated from TDX/M data set related to mowing events.

	TF1 18–23	TF2 7–13	TF3 20–21	TF4 18–23	TF5 9–18
H	$\uparrow 0.061$	$\uparrow 0.061$	$\downarrow 0.041$	$\uparrow 0.034$	$\uparrow 0.012$
$\lvert\gamma_{hhvv}\rvert$	$\downarrow 0.083$	$\downarrow 0.030$	$\uparrow 0.059$	$\uparrow 0.028$	$\downarrow 0.11$
	TF6 3–21	TF7 22–23	TF8 9–18	TF9 9–18	TF10 9–18
H	$\uparrow 0.068$	$\downarrow 0.0041$	$\uparrow 0.018$	$\uparrow 0.062$	$\uparrow 0.018$
$\lvert\gamma_{hhvv}\rvert$	$\uparrow 0.066$	$\downarrow 0.022$	$\downarrow 0.067$	$\downarrow 0.070$	$\downarrow 0.083$

Table 3.7: Changes in H and $|\gamma_{hhvv}|$ parameters calculated from R2 data set related to mowing events.

acquisitions were further in time from the mowing events. In the case of TDX, less time passed on average between the mowing and acquisitions.

From Tables 3.5 and 3.6, it is evident that the results are similar for both the evening and the morning passes of TDX. The difference in the incidence angle is

4.5° (see Table 3.2), but the look direction difference is 158°. In this study, the grasslands had no alignment effects. Thus, the evening and morning passes can be analyzed together given similar incidence angles.

The average increase of H after mowing for the TDX series is 0.07 and the maximum of 0.21 (TDX/E, TF1). For R2, the average increase is 0.029, and the maximum is 0.068 (TF6). The decrease of $|\gamma_{hhvv}|$ was more pronounced. On average, $|\gamma_{hhvv}|$ decreased by 0.12 (TDX) and 0.042 (R2). The maximum decrease was registered as 0.27 (TDX/E, TF1) and 0.11 (R2, TF5).

The magnitude of changes in $|\gamma_{hhvv}|$ and H seems to be related to the amount of vegetation left on the field after mowing. When less than 0.5 kg/m^2 of grass was left after the mowing event, the change of parameters was less pronounced or even in the opposite direction (TF5/1, TF5/2, TF7, TF9, and TF10 for TDX/E, see Publication **III**, Figure 10). Alternatively, when more than 0.5 kg/m^2 of grass was left after the mowing event, the changes were more pronounced – TF1, TF2, TF4, TF8 for TDX/M, and TF1, TF4, TF8 for TDX/E.

The changes in $|\gamma_{hhvv}|$ and H parameters in respect to mowing is explained via the dual polarization particle scattering model [100]. According to the model, the 2×2 T-matrix can be expressed as a function of three parameters [124]:

- f_V – the intensity of the vegetation volume scattering
- A_p – function of particle shape and dielectric constant ($A_p \to 0$ for vertical dipole, $A_p = 1$ for sphere, and $A_p \to \infty$ for horizontal dipole)
- Δ – the orientation randomness parameter ($\Delta = 0°$ for completely oriented particles, and $\Delta = 90°$ for randomly oriented particles)

The $T_{2\times2}$ matrix can be expressed as [124]:

$$
\begin{aligned}
T_{2\times2} &= f_V \begin{bmatrix} T_{11} & T_{12}\frac{\sin 2\Delta}{2\Delta} \\ T_{12}^{*}\frac{\sin 2\Delta}{2\Delta} & T_{22}(1+\frac{\sin 4\Delta}{4\Delta}) \end{bmatrix} \\
T_{11} &= \frac{4}{15}(A_p-1)^2 + \frac{4}{3}(A_p-1) + 2 \\
T_{12} &= \frac{4}{15}(A_p-1)^2 + \frac{2}{3}(A_p-1) \\
T_{22} &= \frac{2}{15}(A_p-1)^2
\end{aligned}
$$

The polarimetric parameters used in the study can be then calculated from the modeled $T_{2\times2}$ matrix. The modeled values of H and $|\gamma_{hhvv}|$ are presented in Figures 3.5 and 3.6, respectively. The vegetation present on the grasslands is approximated

to a dipole-like shape, so that standing vegetation corresponds to $0 < A_p < 1$, and vegetation on the ground corresponds to $1 < A_p < \infty$. The dipole approximation holds as most of the water is contained in the stalks and not the foliage. According to the field surveys, in case of the red clover ≈65% of water is contained in the stalks. Other vegetation species included in the study have an even more pronounced vertical distribution of biomass.

As seen in Figures 3.5 and 3.6, under certain orientation randomness Δ conditions transition from vertical dipoles ($0 < A_p < 1$, standing vegetation) to horizontal dipoles ($1 < A_p < \infty$, cut vegetation lying on the ground) causes an increase of H (left to right side in Figure 3.5) and decrease of $|\gamma_{hhvv}|$ (left to right side in Figure 3.6). This hold true for Δ values larger than $45°$, suggesting that mowing might also increase the width of the orientation distribution.

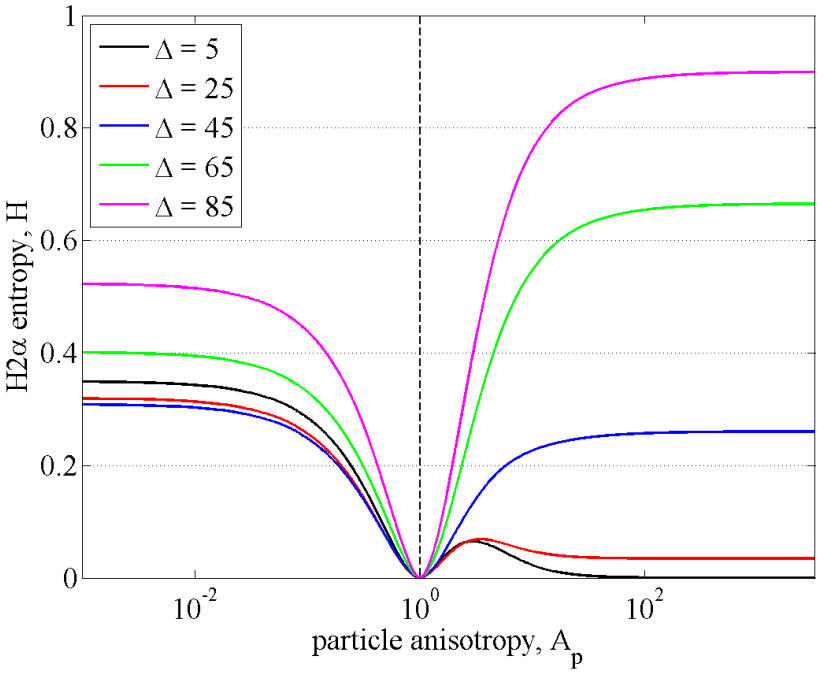

Figure 3.5: H2α entropy H as a function of particle anisotropy A_p (A_p < 1 for vertical dipoles, A_p > 1 for horizontal dipoles) and orientation randomness parameter Δ according to the dual polarization particle scattering model for vegetation [100].

In order to verify that the vegetation model is applicable, surface-to-volume ratios were computed for the grasslands. R2 data were used, and the modified Freeman

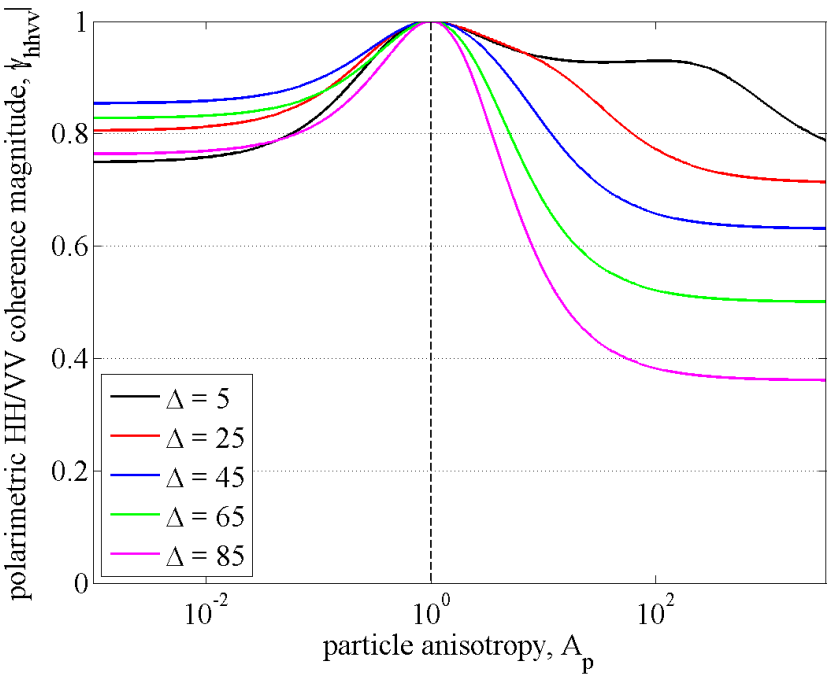

Figure 3.6: Polarimetric HH/VV coherence magnitude $|\gamma_{hhvv}|$ as a function of particle anisotropy A_p (A_p < 1 for vertical dipoles, A_p > 1 for horizontal dipoles) and orientation randomness parameter Δ according to the dual polarization particle scattering model for vegetation [100].

decomposition was applied [125]. Calculated for conditions before and after the mowing, the ratios ranged from ≈–12 dB to ≈–6 dB. This indicates that changes in the polarimetric scattering are most likely caused by the vegetation and not by the surface effects. The same holds for X-band TDX data, as the shorter wavelength (compared to C-band R2) would cause even more volume scattering due to increased interaction with in the vegetation.

A schematic representation of the polarimetric effects in grassland vegetation before and after mowing is presented in Figure 3.7, according to the particle scattering model. Before mowing, the vegetation is predominantly vertical, i.e. most of the biomass is contained in the upright stalks. Additionally, smaller stems and leaves introduce deviation from the upright direction. After mowing, on the other hand, the vegetation left on the ground is predominantly horizontal. The individual plants are randomly positioned introducing orientation randomness. Due to the change of dom-

inant orientation (vertical to horizontal), the observed H2α entropy H increases, and the polarimetric HH/VV coherence magnitude $|\gamma_{hhvv}|$ decreases. The magnitude of the change of H and $|\gamma_{hhvv}|$ parameters depends on the amount of vegetation left on the ground after mowing – more vegetation leads to a larger change. If no vegetation is left, no change is observed, and the scattering partially corresponds to that of bare soil with low H and high $|\gamma_{hhvv}|$ values.

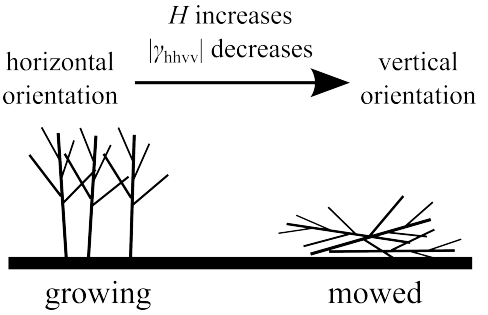

Figure 3.7: Change of vegetation orientation due to mowing and its effect on H and $|\gamma_{hhvv}|$.

3.5. Summary of the study

Grassland vegetation parameters measured during a field survey campaign were analyzed in time series in relation to InSAR and PolSAR parameters calculated from X- and C-band SAR data. The time series were analyzed in respect to two topics – determination of vegetation height, and detection of mowing events.

Vegetation height was found to be correlated to one-day repeat-pass X-band InSAR temporal decorrelation term $|\gamma_t|$, but not to any of the measured PolSAR parameters. Increase of vegetation height decreased the $|\gamma_t|$, and this effect was observed for heights smaller than 0.3 m. Total decorrelation of $|\gamma_t|$ occurred at taller heights. The relationship between $|\gamma_t|$ and the vegetation height was explained via a model based on random motion of scatterers. Using the model and limiting the data set to vegetation shorter than 1 m, strong correlation was established between $|\gamma_t|$ and the vegetation height with a coefficient $r = 0.81$.

Both the InSAR and PolSAR were showed to be capable of detecting mowing events on grasslands. In case of InSAR, the measured one-day repeat-pass X-band InSAR coherence rose steeply after the mowing event due to coherent scattering from the bare soil. However, precipitation and human activities during the one-day temporal baseline limit the use of this method and introduce additional parameters that

have to be taken into account.

Out of several PolSAR parameters analyzed in the study, the HH/VV polarimetric coherence magnitude $|\gamma_{hhvv}|$ and H2α entropy H calculated from the TDX data set showed the most consistent and distinguishable behavior in relation to mowing events. On average, H increased by 7% after mowing and $|\gamma_{hhvv}|$ decreased by 12%. The magnitude of changes was dependent on the amount of vegetation left on the field after mowing, with the effect being stronger for larger amounts. Changes in H and $|\gamma_{hhvv}|$ parameters after mowing were explained by a vegetation particle scattering model. According to the model, change of the orientation and the randomness of the vegetation causes changes in the polarimetric parameters.

4. CONCLUSIONS AND FUTURE WORK

This work investigates how data from advanced space borne SAR sensors can be used to improve and create new applications for the remote sensing of complex natural environments. Advances in technology and signal processing have allowed for the development of high resolution SAR sensors that operate in several modes and configurations. The data they provide can be used to investigate complex environments, such as forest floods and agricultural grasslands. The aim of this work is to investigate possible advances in two SAR applications – mapping of forest floods, and monitoring of agricultural grasslands. The approaches presented here can help to develop more precise flood mapping algorithms, and to create first operational grassland monitoring systems. This work is presented in two main chapters. Chapter 2 is devoted to flood detection in forested areas. Chapter 3 focuses on grasslands, and investigates the possibility to detect mowing events and determine the vegetation height.

The use of polarimetric HH–VV channel and HH/VV phase difference offers improvement for delineating between flooded and unflooded forest areas. The approach is based on the polarimetric phase shift due to double-bounce scattering that occurs between the tree trunk and water surface under the canopy. The proposed approach yielded higher backscatter difference between flooded and unflooded conditions than using the HH channel. The improvement was more pronounced for deciduous cases, ranging from 1 to 1.6 dB. In case of coniferous forest, the difference was less than 1 dB on average. In future studies, using longer wavelengths than X-band and shallower incidence angles close to 45° would yield better results with the same technique. Improved penetration of longer wavelengths will mean more signal reaching the trunk-surface layer, and shallower incidence angles would maximize the phase shift leading to higher HH–VV backscatter levels.

In the second part of this work, it is shown that advanced InSAR and PolSAR techniques are capable of providing information about the vegetation height and mowing events in certain conditions. Coherence computed for interferometric pairs with one-day temporal baseline is shown to be strongly correlated to vegetation height. However, the relation holds for relatively short vegetation, up to $\approx$0.25 cm. Continuation studies should focus on using longer wavelengths than those in the study (X-band) and, if possible, shorter temporal baselines. Such approach should increase the range of vegetation heights that could be detected with the presented approach. The interferometric coherence is also shown to be able to provide information about mowing events on grasslands. Human activity and precipitation, however, hampers the use of this approach and care must be taken to account for these

phenomena in the future. A couple of PolSAR parameters are found to be capable of detecting mowing in case some vegetation is left on the ground after the event. Change of dominant orientation in the vegetation from vertical to horizontal due to mowing causes a detectable change in HH/VV polarimetric coherence magnitude and H2α entropy. The magnitude of change is related to the amount of vegetation left on the ground. The results offer a starting point for future studies focused on developing applications for monitoring of agricultural grasslands.

REFERENCES

[1] R.A. Hanel, J. Licht, W. Nordberg, R.A. Stampfl, and W.G. Stroud, "The Satellite Vanguard II: Cloud Cover Experiment," *IRE Trans. Military Electron.*, vol. MIL-4, no. 2-3, pp. 245–247, April 1960.

[2] M. Richter, "The Design of a Resources Survey System," *IEEE Trans. Geosci. Electron.*, vol. 7, no. 4, pp. 200–205, Oct 1969.

[3] J.W. Rouse and S. Riter, "Erts Experiments," *IEEE Trans. Geosci. Electron.*, vol. 11, no. 1, pp. 3–76, Jan 1973.

[4] J. Dunne, "The seasat-a project: An overview," in *OCEANS '76*, Sept 1976, pp. 217–221.

[5] D.B. Lame and G.H. Born, "SEASAT measurement system evaluation: Achievements and limitations," *J. Geoph. Res.: Oceans*, vol. 87, no. C5, pp. 3175–3178, 1982.

[6] C.A. Wiley, "Synthetic Aperture Radars," *IEEE Trans. Aerosp. Electron. Syst.*, vol. AES-21, no. 3, pp. 440–443, May 1985.

[7] C.W. Sherwin, J.P. Ruina, and R.D. Rawcliffe, "Some Early Developments in Synthetic Aperture Radar Systems," *Military Electronics, IRE Trans.*, vol. MIL-6, no. 2, pp. 111–115, April 1962.

[8] J.J. Kovaly, *Synthetic Aperture Radar*, Radar Library. Artech House, 1976.

[9] I. Cumming and J.R. Bennett, "Digital processing of Seasat SAR data," in *Acoustics, Speech, and Signal Processing, IEEE International Conference on ICASSP '79.*, Apr 1979, vol. 4, pp. 710–718.

[10] Jr. McCandles, S.W., "The origin, evolution and legacy of SEASAT," in *Geoscience and Remote Sensing Symposium, 2003. IGARSS '03. Proceedings. 2003 IEEE International*, July 2003, vol. 1, pp. 32–34 vol.1.

[11] V.S. Etkin, K.T. Litovchenko, A.V. Smirnov, and M.A. Naumenko, "Investigations of radar signatures of lake surface with the "COSMOS-1870" ("ALMAZ-0") SAR," in *Geoscience and Remote Sensing Symposium, 1992. IGARSS '92. International*, May 1992, vol. 2, pp. 1774–1776.

[12] C. Elachi, J. Cimino, and M. Settle, "Overview of the shuttle imaging radar-B preliminary scientific results," *Science (New York, N.Y.)*, vol. 232, no. 4757, pp. 1511–1516, June 1986.

[13] J. Cimino, C. Elachi, and M. Settle, "SIR-B-The Second Shuttle Imaging Radar Experiment," *IEEE Trans. Geosci. Remote Sens.*, vol. GE-24, no. 4, pp. 445–452, July 1986.

[14] J. Way and E.A. Smith, "The evolution of synthetic aperture radar systems and their progression to the EOS SAR," *IEEE Trans. Geosci. Remote Sens.*, vol. 29, no. 6, pp. 962–985, Nov 1991.

[15] J.C. Curlander, B. Holt, and K. Hussey, "Determination of sea ice motion using digital SAR imagery," *IEEE J. Ocean. Eng.*, vol. 10, no. 4, pp. 358–367, Oct 1985.

[16] J.F. Vesecky, R. Samadani, M.P. Smith, J.M. Daida, and R.N. Bracewell, "Observation of sea-ice dynamics using synthetic aperture radar images: automated analysis," *IEEE Trans. Geosci. Remote Sens.*, vol. 26, no. 1, pp. 38–48, Jan 1988.

[17] M. Barni, M. Betti, and A. Mecocci, "A fuzzy approach to oil spill detection an SAR images," in *Geoscience and Remote Sensing Symposium, 1995. IGARSS '95. 'Quantitative Remote Sensing for Science and Applications', International*, Jul 1995, vol. 1, pp. 157–159 vol.1.

[18] F.T. Ulaby, F. Kouyate, B. Brisco, and T.H.L. Williams, "Textural Infornation in SAR Images," *IEEE Trans. Geosci. Remote Sens.*, vol. GE-24, no. 2, pp. 235–245, March 1986.

[19] A.C. Bovik, "On detecting edges in speckle imagery," *IEEE Trans. Acoust., Speech, Signal Process.*, vol. 36, no. 10, pp. 1618–1627, Oct 1988.

[20] R. Bamler and P. Hartl, "Synthetic aperture radar interferometry," *Inverse Problems*, vol. 14, no. 4, pp. R1, 1998.

[21] R.M. Goldstein, H.A. Zebker, and C.L. Werner, "Satellite radar interferometry: Two-dimensional phase unwrapping," *Radio Science*, vol. 23, no. 4, pp. 713–720, 1988.

[22] Fuk K.Li and R.M. Goldstein, "Studies of multibaseline spaceborne interferometric synthetic aperture radars," *IEEE Trans. Geosci. Remote Sens.*, vol. 28, no. 1, pp. 88–97, Jan 1990.

[23] R.G. Blom, R.E. Crippen, and C. Elachi, "Detection of subsurface features in SEASAT radar images of Means Valley, Mojave Desert, California," *Geology*, vol. 12, no. 6, pp. 346–349, 1984.

[24] J.F. McCauley, G..G Schaber, C.S. Breed, M.J. Grolier, C.V. Haynes, B. Issawi, C. Elachi, and R. Blom, "Subsurface Valleys and Geoarcheology of the Eastern Sahara Revealed by Shuttle Radar," *Science*, vol. 218, no. 4576, pp. 1004–1020, 1982.

[25] C. Elachi, L.E. Roth, and Gerald G. Schaber, "Spaceborne Radar Subsurface Imaging in Hyperarid Regions," *IEEE Trans. Geosci. Remote Sens.*, vol. GE-22, no. 4, pp. 383–388, July 1984.

[26] C. Elachi and J. Granger, "Aerospace: Spaceborne imaging radars probe 'in depth': New spaceborne radar sensors allow all-weather, day or night, high-resolution imaging of the earth's land and ocean surfaces," *IEEE Spectr.*, vol. 19, no. 11, pp. 24–29, Nov 1982.

[27] Shih-Tseng Wu, "Analysis of synthetic aperture radar data acquired over a variety of land cover," *IEEE Trans. Geosci. Remote Sens.*, vol. GE-22, no. 6, pp. 550–557, Nov 1984.

[28] Shih-Tseng Wu, "Potential Application of Multipolarization SAR for Pine-Plantation Biomass Estimation," *IEEE Trans. Geosci. Remote Sens.*, vol. GE-25, no. 3, pp. 403–409, May 1987.

[29] H. C. MacDonald, W. P. Waite, and J. S. Demarcke, "Use of Seasat satellite radar imagery for the detection of standing water beneath forest vegetation," in *Proc. Amer. Soc. Photogramm. Annu. Tech. Meeting*, Oct 1980, pp. RS–3–B–1–RS–3–B–13.

[30] F.T. Ulaby, Brian Brisco, and C. Dobson, "Improved Spatial Mapping of Rainfall Events with Spaceborne SAR Imagery," *IEEE Trans. Geosci. Remote Sens.*, vol. GE-21, no. 1, pp. 118–121, Jan 1983.

[31] B. J. Blanchard and A. T. C. Chang, "Estimation of Soil Moisture from SEASAT SAR data," *JAWRA Journal of the American Water Resources Association*, vol. 19, no. 5, pp. 803–810, 1983.

[32] J.R. Wang, E.T. Engmen, James C. Shiue, M. Rusek, and C. Steinmeier, "The SIR-B Observations of Microwave Backscatter Dependence on Soil Moisture, Surface Roughness, and Vegetation Covers," *IEEE Trans. Geosci. Remote Sens.*, vol. GE-24, no. 4, pp. 510–516, July 1986.

[33] M.C. Dobson and F.T. Ulaby, "Preliminaly Evaluation of the SIR-B Response to Soil Moisture, Surface Roughness, and Crop Canopy Cover," *IEEE Trans. Geosci. Remote Sens.*, vol. GE-24, no. 4, pp. 517–526, July 1986.

[34] N.H. Herman, R.L. Jordan, and E.R. Caro, "SIR-C flight hardware: design objectives, actual performance, and suggestions for future applications," in *Geoscience and Remote Sensing Symposium, 1995. IGARSS '95. 'Quantitative Remote Sensing for Science and Applications', International*, Jul 1995, vol. 3, pp. 2047–2050 vol.3.

[35] G. Duchossois and C. Honvault, "The First ESA Remote Sensing Satellite (ERS)–The Programme and the System," in *OCEANS 81*, Sept 1981, pp. 1014–1018.

[36] Y. Nemoto, H. Nishino, M. Ono, Hitoshi Mizutamari, K. Nishikawa, and K. Tanaka, "Japanese Earth Resources Satellite-1 synthetic aperture radar," *IEEE Proc.*, vol. 79, no. 6, pp. 800–809, Jun 1991.

[37] G. Duchossois and P. Martin, "ERS-1 and ERS-2 Tandem Operations," *ESA Bulletin - European Space Agency*, , no. 83, pp. 54–60, AUG 1995.

[38] A. Mahmood, "RADARSAT-1 Background Mission for a global SAR coverage," in *Geoscience and Remote Sensing, 1997. IGARSS '97. Remote Sensing - A Scientific Vision for Sustainable Development., 1997 IEEE International*, Aug 1997, vol. 3, pp. 1217–1219 vol.3.

[39] Y.-L. Desnos, H. Laur, P. Lim, P. Meisl, and T. Gach, "The ENVISAT-1 Advanced Synthetic Aperture Radar processor and data products," in *Geoscience and Remote Sensing Symposium, 1999. IGARSS '99 Proceedings. IEEE 1999 International*, 1999, vol. 3, pp. 1683–1685 vol.3.

[40] J.-S. Lee and E. Pottier, *Polarimetric radar imaging: from basics to applications*, Optical Science and Engineering, 143. Taylor & Francis, Hoboken, NJ, 2009.

[41] W.-M. Boerner, M. El-Arini, Chung-Yee Chan, and P. Mastoris, "Polarization dependence in electromagnetic inverse problems," *IEEE Trans. Antennas Propag.*, vol. 29, no. 2, pp. 262–271, Mar 1981.

[42] G. Sinclair, "The Transmission and Reception of Elliptically Polarized Waves," *IRE Proc.*, vol. 38, no. 2, pp. 148–151, Feb 1950.

[43] E.M. Kennaugh, *Polarization Properties of Radar Reflections*, Ohio State University, 1952.

[44] J.R. Huynen, *Phenomenological theory of radar targets*, Drukkerij Bronder-Offset N.V., 1970.

[45] R Shibasaki, Y Osawa, K Toda, H Wakabayashi, T Hamazaki, and H Takamatsu, "Advanced land observing satellite (ALOS): Mission objectives and payloads," in *Advanced and Next-Generation Satellites II*, 1997, vol. 2957, pp. 200–207.

[46] A. Moreira, "A golden age for spaceborne SAR systems," in *Microwaves, Radar, and Wireless Communication (MIKON), 2014 20th International Conference on*, June 2014, pp. 1–4.

[47] A.A. Thompson, A.P. Luscombe, K. James, and P. Fox, "New modes and techniques of the RADARSAT-2 SAR," in *Geoscience and Remote Sensing Symposium, 2001. IGARSS '01. IEEE 2001 International*, 2001, vol. 1, pp. 485–487.

[48] M. Stangl, R. Werninghaus, B. Schweizer, C. Fischer, M. Brandfass, J. Mittermayer, and H. Breit, "TerraSAR-X technologies and first results," *IEE Proc. Radar, Sonar and Navigation*, vol. 153, no. 2, pp. 86–95, April 2006.

[49] A. Moreira, G. Krieger, I. Hajnsek, D. Hounam, M. Werner, S. Riegger, and E. Settelmeyer, "TanDEM-X: a TerraSAR-X add-on satellite for single-pass SAR interferometry," in *Geoscience and Remote Sensing Symposium, 2004. IGARSS '04. Proceedings. 2004 IEEE International*, Sept 2004, vol. 2, pp. 1000–1003 vol.2.

[50] F. Caltagirone, P. Spera, R. Vigliotti, and G. Manoni, "SkyMed/COSMO mission overview," in *Geoscience and Remote Sensing Symposium Proceedings, 1998. IGARSS '98. 1998 IEEE International*, Jul 1998, vol. 2, pp. 683–685 vol.2.

[51] P. Snoeij, E. Attema, M. Davidson, B. Duesmann, N. Floury, G. Levrini, B. Rommen, and B. Rosich, "Sentinel-1 radar mission: Status and performance," *IEEE Trans. Aerosp. Electron. Syst.*, vol. 25, no. 8, pp. 32–39, Aug 2010.

[52] H. Bach, F. Appel, K. Fellah, and P. de Fraipont, "Application of flood monitoring from satellite for insurances," in *Geoscience and Remote Sensing Symposium, 2005. IGARSS '05. Proceedings. 2005 IEEE International*, July 2005, vol. 1, pp. 4 pp.–.

[53] J. Sanyal and X.X. Lu, "Application of Remote Sensing in Flood Management with Special Reference to Monsoon Asia: A Review," *Natural Hazards*, vol. 33, no. 2, pp. 283–301, 2004.

[54] H. Rasid and M.A.H. Pramanik, "Areal extent of the 1988 flood in Bangladesh: How much did the satellite imagery show?," *Natural Hazards*, vol. 8, no. 2, pp. 189–200, 1993.

[55] J.L. Place, "Mapping of forested wetland: use of Seasat radar images to complement conventional sources (USA).," *Professional Geographer*, vol. 37, no. 4, pp. 463–469, 1985, cited By 0.

[56] F. Messner, "Evaluating flood damages: guidance and recommendations on principles and methods," Tech. Rep., Helmholz Unweltforschungszentrum (UFZ), 2007.

[57] T. T. Kozlowski, "Responses of woody plants to flooding and salinity," *Tree Physiology*, vol. 17, no. 7, pp. 490, 1997.

[58] K.D. Coder and Daniel B. Warnell School of Forest Resources, *Flood Damage to Trees*, Extension Publication / University of Georgia School of Forest Resources. University of Georgia, D.B. Warnell School of Forest Resources, 1994.

[59] J.P. Ormsby, B.J. Blanchard, and A.J. Blanchard, "Detection of Lowland Flooding using Aactive Microwave Systems," *Photogram. Eng. Rem. Sens.*, vol. 51, no. 3, pp. 317–328, 1985.

[60] L.L. Hess, J.M. Melack, S. Filoso, and Y. Wang, "Delineation of inundated area and vegetation along the Amazon floodplain with the SIR-C synthetic aperture radar," *IEEE Trans. Geosci. Remote Sens.*, vol. 33, no. 4, pp. 896–904, Jul 1995.

[61] J.J. van Zyl, "Unsupervised classification of scattering behavior using radar polarimetry data," *IEEE Trans. Geosci. Remote Sens.*, vol. 27, no. 1, pp. 36–45, Jan 1989.

[62] M.C. Dobson, F.T. Ulaby, L.E. Pierce, T.L. Sharik, K.M. Bergen, J. Kellndorfer, J.R. Kendra, E. Li, Y.C. Lin, A. Nashashibi, K. Sarabandi, and P. Siqueira, "Estimation of forest biophysical characteristics in Northern Michigan with SIR-C/X-SAR," *IEEE Trans. Geosci. Remote Sens.*, vol. 33, no. 4, pp. 877–895, Jul 1995.

[63] Y. Wang, L.L. Hess, S. Filoso, and J.M. Melack, "Understanding the radar backscattering from flooded and nonflooded Amazonian forests: Results from canopy backscatter modeling," *Rem. Sens. Env.*, vol. 54, no. 3, pp. 324 – 332, 1995.

[64] E.S. Kasischke and L.L. BourgeauChavez, "Monitoring South Florida wetlands using ERS-1 SAR imagery," *Photogram. Eng. Rem. Sens.*, vol. 63, no. 3, pp. 281–291, Mar 1997.

[65] K.O. Pope, E. Rejmankova, J.F. Paris, and R. Woodruff, "Detecting seasonal flooding cycles in marshes of the Yucatan Peninsula with SIR-C polarimetric radar imagery," *Rem. Sens. Env.*, vol. 59, no. 2, pp. 157 – 166, 1997, Spaceborne Imaging Radar Mission.

[66] Y. Wang and M.L. Imhoff, "Simulated and Observed L-HH Radar Backscatter from Tropical Mangrove Forests," *Int. J. Rem. Sens.*, vol. 14, no. 15, pp. 2819–2828, Oct 1993.

[67] M.W. Lang, P.A. Townsend, and E.S. Kasischke, "Influence of incidence angle on detecting flooded forests using C-HH synthetic aperture radar data," *Rem. Sens. Env.*, vol. 112, no. 10, pp. 3898 – 3907, 2008.

[68] K. Voormansik, J. Praks, O. Antropov, J. Jagomagi, and K. Zalite, "Flood Mapping With TerraSAR-X in Forested Regions in Estonia," *IEEE J. Sel. Topics Appl. Earth Obs. Rem. Sens.*, vol. 7, no. 2, pp. 562–577, Feb 2014.

[69] F.T. Ulaby, D. Held, M.C. Donson, K.C. McDonald, and T.B.A. Senior, "Relating Polaization Phase Difference of SAR Signals to Scene Properties," *IEEE Trans. Geosci. Remote Sens.*, vol. GE-25, no. 1, pp. 83–92, Jan 1987.

[70] M.T. Svendsen, H. Skriver, and A. Thomsen, "Investigation of polarimetric SAR data acquired at multiple incidence angles," in *Geoscience and Remote Sensing Symposium Proceedings, 1998. IGARSS '98. 1998 IEEE International*, Jul 1998, vol. 3, pp. 1720–1722 vol.3.

[71] T. Le Toan, A. Beaudoin, J. Riom, and D. Guyon, "Relating forest biomass to SAR data," *IEEE Trans. Geosci. Remote Sens.*, vol. 30, no. 2, pp. 403–411, Mar 1992.

[72] H.J. Smit, M.J. Metzger, and F. Ewert, "Spatial distribution of grassland productivity and land use in Europe," *Agricultural Systems*, vol. 98, no. 3, pp. 208 – 219, 2008.

[73] A. Hopkins and B. Holz, "Grassland for agriculture and nature conservation: production, quality and multi-functionality," in *Integrating Efficient Grassland Farming and Biodiversity*, Lillak, R and Viiralt, R and Linke, A and Geherman, V, Ed. European Grassland Federation, 2005, vol. 10 of *Grassland Science in Europe*, pp. 15–29.

[74] A. Ruimy, B. Saugier, and G. Dedieu, "Methodology for the estimation of terrestrial net primary production from remotely sensed data," *J. Geoph. Res.: Atmospheres*, vol. 99, no. D3, pp. 5263–5283, 1994.

[75] M.S. Moran, Y. Inoue, and E.M. Barnes, "Opportunities and limitations for image-based remote sensing in precision crop management," *Rem. Sens. Env.*, vol. 61, no. 3, pp. 319 – 346, 1997.

[76] W.G.M Bastiaanssen, D.j. Molden, and I.W. Makin, "Remote sensing for irrigated agriculture: examples from research and possible applications," *Agricultural Water Management*, vol. 46, no. 2, pp. 137 – 155, 2000.

[77] P.M. Hansen and J.K. Schjoerring, "Reflectance measurement of canopy biomass and nitrogen status in wheat crops using normalized difference vegetation indices and partial least squares regression," *Rem. Sens. Env.*, vol. 86, no. 4, pp. 542 – 553, 2003.

[78] T. Le Toan, F. Ribbes, Li-Fang Wang, N. Floury, Kung-Hau Ding, Jin Au Kong, M. Fujita, and T. Kurosu, "Rice crop mapping and monitoring using ERS-1 data based on experiment and modeling results," *IEEE Trans. Geosci. Remote Sens.*, vol. 35, no. 1, pp. 41–56, Jan 1997.

[79] F. Mattia, T. Le Toan, G. Picard, F.I. Posa, A. D'Alessio, C. Notarnicola, A.M. Gatti, M. Rinaldi, G. Satalino, and G. Pasquariello, "Multitemporal C-band radar measurements on wheat fields," *IEEE Trans. Geosci. Remote Sens.*, vol. 41, no. 7, pp. 1551–1560, July 2003.

[80] C. Rossi and E. Erten, "Paddy-Rice Monitoring Using TanDEM-X," *IEEE Trans. Geosci. Remote Sens.*, vol. 53, no. 2, pp. 900–910, Feb 2015.

[81] F. Del Frate, G. Schiavon, D. Solimini, M. Borgeaud, D.H. Hoekman, and M.A.M. Vissers, "Crop classification using multiconfiguration C-band SAR data," *IEEE Trans. Geosci. Remote Sens.*, vol. 41, no. 7, pp. 1611–1619, July 2003.

[82] Xin Tian, Erxue Chen, Zengyuan Li, Z.B. Su, Feilong Ling, Lina Bai, and Fengyu Wang, "Comparison of crop classification capabilities of spaceborne

multi-parameter SAR data," in *Geoscience and Remote Sensing Symposium (IGARSS), 2010 IEEE International*, July 2010, pp. 359–362.

[83] B. Barrett, I. Nitze, S. Green, and F. Cawkwell, "Assessment of multi-temporal, multi-sensor radar and ancillary spatial data for grasslands monitoring in ireland using machine learning approaches," *Rem. Sens. Env.*, vol. 152, pp. 109 – 124, 2014.

[84] U. Wegmuller and C. Werner, "Retrieval of vegetation parameters with SAR interferometry," *IEEE Trans. Geosci. Remote Sens.*, vol. 35, no. 1, pp. 18–24, Jan 1997.

[85] C. Schuster, I. Ali, P. Lohmann, A. Frick, M. Forster, and B. Kleinschmit, "Towards Detecting Swath Events in TerraSAR-X Time Series to Establish NATURA 2000 Grassland Habitat Swath Management as Monitoring Parameter," *Remote Sensing*, vol. 3, no. 7, pp. 1308, 2011.

[86] I. Ali, C. Schuster, M. Zebisch, M. Forster, B. Kleinschmit, and C. Notarnicola, "First Results of Monitoring Nature Conservation Sites in Alpine Region by Using Very High Resolution (VHR) X-Band SAR Data," *Selected Topics in Applied Earth Observations and Remote Sensing, IEEE Journal of*, vol. 6, no. 5, pp. 2265–2274, Oct 2013.

[87] J. Gray, "The Common Agricultural Policy and the Re-Invention of the Rural in the European Community," *Sociologia Ruralis*, vol. 40, no. 1, pp. 30–52, 2000.

[88] M.J. Hill, G.E. Donald, and P.J. Vickery, "Relating radar backscatter to biophysical properties of temperate perennial grassland," *Rem. Sens. Env.*, vol. 67, no. 1, pp. 15 – 31, 1999.

[89] M. Herold, C.C. Schmullius, and I. Hajnsek, "Multifrequency and Polarimetric Radar Remote Sensing of Grassland-Geobiophysical and Landcover Parameter Retrieval with E-SAR Data," *Decade of Trans-European Remote Sensing Cooperation*, 2001.

[90] N. Mino, G. Saito, and S. Ogawa, "Detecting management practices of improved grasslands using ERS-1 SAR data," *Journal of the Japan society of photogrammetry and remote sensing*, vol. 37, no. 4, pp. 23–33, 1998.

[91] K. Voormansik, T. Jagdhuber, A. Olesk, I. Hajnsek, and K.P. Papathanassiou, "Towards a detection of grassland cutting practices with dual polarimetric TerraSAR-X data," *Int. J. Rem. Sens.*, vol. 34, no. 22, pp. 8081–8103, 2013.

[92] J.I.H. Askne, P.B.G. Dammert, L.M.H. Ulander, and G. Smith, "C-band repeat-pass interferometric SAR observations of the forest," *IEEE Trans. Geosci. Remote Sens.*, vol. 35, no. 1, pp. 25–35, Jan 1997.

[93] J. Askne, M. Santoro, G. Smith, and J.E.S. Fransson, "Multitemporal repeat-pass SAR interferometry of boreal forests," *IEEE Trans. Geosci. Remote Sens.*, vol. 41, no. 7, pp. 1540–1550, July 2003.

[94] J. Praks, M. Hallikainen, O. Antropov, and D. Molina, "Boreal forest tree height estimation from interferometric TanDEM-X images," in *Geoscience and Remote Sensing Symposium (IGARSS), 2012 IEEE International*, July 2012, pp. 1262–1265.

[95] X Blaes and P Defourny, "Retrieving crop parameters based on tandem ERS 1/2 interferometric coherence images," *Rem. Sens. Env.*, vol. 88, no. 4, pp. 374–385, DEC 30 2003.

[96] S.R. Cloude and E. Pottier, "An entropy based classification scheme for land applications of polarimetric SAR," *IEEE Trans. Geosci. Remote Sens.*, vol. 35, no. 1, pp. 68–78, Jan 1997.

[97] S. Cloude, "The dual polarization entropy/alpha decomposition: a PALSAR case study," in *ESA Special Publication*, 2007, vol. 644, p. 2.

[98] P.A. Townsend, "Relationships between forest structure and the detection of flood inundation in forested wetlands using C-band SAR," *In. J. Rem. Sens.*, vol. 23, no. 3, pp. 443–460, 2002.

[99] P. Beckmann and A. Spizzichino, *The scattering of electromagnetic waves from rough surfaces*, Norwood, MA : Artech House, 1987.

[100] S. Cloude, *Polarisation: applications in remote sensing*, Oxford University Press, 2009.

[101] Y. Wang and F.W. Davis, "Decomposition of polarimetric synthetic aperture radar backscatter from upland and flooded forests," *In. J. Rem. Sens.*, vol. 18, no. 6, pp. 1319–1332, 1997.

[102] J.A. Stratton, *Electromagnetic theory*, John Wiley & Sons, 2007.

[103] M.S. Horritt, D.C. Mason, D.M. Cobby, I.J. Davenport, and P.D. Bates, "Waterline mapping in flooded vegetation from airborne SAR imagery," *Rem. Sens. Env.*, vol. 85, no. 3, pp. 271 – 281, 2003.

[104] lkan Mo and J.R. Wang, "Modelling Of Sar Polarisation Phase Difference From Trees," in *Geoscience and Remote Sensing Symposium, 1988. IGARSS '88. Remote Sensing: Moving Toward the 21st Century., International*, Sept 1988, vol. 1, pp. 55–58.

[105] "Estonian Meteorological and Hydrological Institute," `http://www.emhi.ee/`.

[106] "Eesti Metsaregister," `http://register.metsad.ee/avalik/`.

[107] A. Toure, K.P.B. Thomson, G. Edwards, R.J. Brown, and B.G. Brisco, "Adaptation of the MIMICS backscattering model to the agricultural context-wheat and canola at L and C bands," *IEEE Trans. Geosci. Remote Sens.*, vol. 32, no. 1, pp. 47–61, Jan 1994.

[108] S.S. Saatchi, R.H. Lang, and D.M. LeVine, "Microwave Backscattering And Emission Model For Grass Canopies," in *Geoscience and Remote Sensing Symposium, 1991. IGARSS '91. Remote Sensing: Global Monitoring for Earth Management., International*, Jun 1991, vol. 4, pp. 1889–1892.

[109] J. Shi, J.J. van Zyl, J.V. Soares, and E.T. Engman, "Retrieval Bare-Soil Moisture Using L-Band SAR," in *XVIIth ISPRS Congress*, 1992, vol. XXIX, pp. 595–597.

[110] D.L. Evans, T.G. Farr, J.J. van Zyl, and H.A. Zebker, "Radar polarimetry: analysis tools and applications," *Geoscience and Remote Sensing, IEEE Transactions on*, vol. 26, no. 6, pp. 774–789, Nov 1988.

[111] Y.-C. Lin and K. Sarabandi, "A Monte Carlo coherent scattering model for forest canopies using fractal-generated trees," *Geoscience and Remote Sensing, IEEE Transactions on*, vol. 37, no. 1, pp. 440–451, Jan 1999.

[112] H. Poorter, K.J. Niklas, P.B. Reich, J. Oleksyn, P. Poot, and L. Mommer, "Biomass allocation to leaves, stems and roots: meta-analyses of interspecific variation and environmental control," *New Phytologist*, vol. 193, no. 1, pp. 30–50, 2012.

[113] U. Wegmuller and C.L. Werner, "SAR interferometric signatures of forest," *IEEE Trans. Geosci. Remote Sens.*, vol. 33, no. 5, pp. 1153–1161, Sep 1995.

[114] E. Rodriguez and J.M. Martin, "Theory and design of interferometric synthetic aperture radars," *Radar and Signal Processing, IEE Proc. F*, vol. 139, no. 2, pp. 147–159, Apr 1992.

[115] H.A. Zebker and J. Villasenor, "Decorrelation in interferometric radar echoes," *IEEE Trans. Geosci. Remote Sens.*, vol. 30, no. 5, pp. 950–959, Sep 1992.

[116] J.-S. Lee, K.W. Hoppel, S.A. Mango, and A.R. Miller, "Intensity and phase statistics of multilook polarimetric and interferometric SAR imagery," *IEEE Trans. Geosci. Remote Sens.*, vol. 32, no. 5, pp. 1017–1028, Sep 1994.

[117] D. Just and R. Bamler, "Phase statistics of interferograms with applications to synthetic aperture radar," *Appl. Opt.*, vol. 33, no. 20, pp. 4361–4368, Jul 1994.

[118] F. Lombardini, F. Bordoni, and F. Gini, "Feasibility study of along-track SAR interferometry with the COSMO-Skymed satellite system," in *Geosci. Remote Sens. Symp., 2004. IGARSS '04. Proc. 2004 IEEE Int.*, Sept 2004, vol. 5, pp. 3337–3340 vol.5.

[119] R. Touzi and A. Lopes, "Statistics of the Stokes parameters and of the complex coherence parameters in one-look and multilook speckle fields," *IEEE Trans. Geosci. Remote Sens.*, vol. 34, no. 2, pp. 519–531, Mar 1996.

[120] E. Renaudin, B. Mercer, Q. Zhang, and M. J. Collins, "Biomass Estimation Using Vertical Forest Structure from SAR Tomography: a Case Study in Canadian Boreal Forest," *ISPRS - Int. Archives of the Photogrammetry, Remote Sens. and Spatial Information Sci.*, vol. XXXIX-B8, pp. 431–435, 2012.

[121] M.E. Engdahl, M. Borgeaud, and M. Rast, "The use of ERS-1/2 Tandem interferometric coherence in the estimation of agricultural crop heights," *IEEE Trans. Geosci. Remote Sens.*, vol. 39, no. 8, pp. 1799–1806, Aug 2001.

[122] "Estonian Land Board Geoportal," `http://geoportaal.maaamet.ee/`.

[123] T. Jagdhuber, I. Hajnsek, and .P Papathanassiou, "Polarimetric Soil Moisture Retrieval at Short Wavelength," in *Proc. of PolInSAR Conference*, 2013, pp. 1–6.

[124] T. Jagdhuber, *Soil parameter retrieval under vegetation cover using SAR polarimetry*, Ph.D. thesis, University of Potsdam, 7 2012.

[125] Y. Yamaguchi, Y. Yajima, and H. Yamada, "A four-component decomposition of POLSAR images based on the coherency matrix," *Geoscience and Remote Sensing Letters, IEEE*, vol. 3, no. 3, pp. 292–296, July 2006.

SUMMARY

This thesis presents research about the application of radar remote sensing for monitoring of complex natural environments, such as flooded forests and agricultural grasslands. The study was carried out in Tartu Observatory, University of Tartu, Ventspils University College, and Aalto University. The research consists of two distinctive parts devoted to polarimetric analysis of images from a seasonal flooding of wetlands, and to polarimetric and interferometric analysis of a summer-long campaign covering eleven agricultural grasslands.

TerraSAR-X data from 2012 were used to assess the use of the double-bounce scattering mechanism for improving the mapping of flooded forest areas. The study confirmed that the HH–VV polarimetric channel that is sensitive to double-bounce scattering provides increased separation between flooded and unflooded forest areas when compared to the conventional HH channel. The increase in separation increases with decreasing forest height, and it is more pronounced for deciduous forests due to the leaf-off conditions during the study. The phase difference information provided by the HH–VV channel may provide additional information for delineating flooded and unflooded forest areas.

Time series of X-band (TanDEM-X and COSMO-SkyMed) and C-band (RADARSAT-2) data from 2013 were analyzed in respect to vegetation parameters collected during a field survey. The one-day repeat-pass X-band interferometric coherence was shown to be correlated to the grassland vegetation height. The coherence was also found to be potentially useful for detecting mowing events. The polarimetric analysis of TanDEM-X and RADARSAT-2 data identified two parameters sensitive to mowing events - the HH/VV polarimetric coherence magnitude and the H2α entropy. Mowing of vegetation consistently caused the coherence magnitude to decrease and the entropy to increase. The effect was more pronounced in case of X-band data. Additionally, the effect was stronger with more vegetation left on the ground after mowing. The effect was explained using a vegetation particle scattering model. The changes in polarimetric variables was shown to be caused by the change of orientation and the randomness of the vegetation.

KOKKUVÕTE (SUMMARY IN ESTONIAN)

Radarkaugseire rakendused metsaüleujutuste ja põllumajanduslike rohumaade jälgimiseks

Käesolev doktoritöö keskendub radarkaugseire rakenduste arendamisele kahes keerukas looduskeskkonnas: üleujutatud metsas ja põllumajanduslikel rohumaadel. Uurimistöö viidi läbi Tartu Observatooriumis, Tartu Ülikoolis, Ventspilsi Kõrgkoolis ja Aalto Ülikoolis. Töö esimene osa käsitleb X-laineala polarimeetrilise radarisignaali käitumist regulaarselt üleujutatavas metsas Soomaa näitel ning teine osa põllumajanduslike rohumaade seisundi ja polarimeetriliste ning interferomeetriliste tehisava-radari parameetrite vahelisi seoseid.

2012 kevadel Soomaa testalal TerraSAR-X andmetega läbi viidud eksperiment näitas, et topelt-peegeldusele tundlik HH-VV polarimeetriline kanal pakub tõesti kontrastsemat tagasihajumisepõhist üleujutatud metsa eristust üleujutamata metsast kui traditsiooniline HH polarimeetriline kanal. HH-VV kanali eelis HH kanali ees on seda suurem, mida madalam on mets ning raagus tingimustes lehtmetsas oli HH-VV kanali eelis HH kanali ees suurem kui okasmetsas. Lisaks on üleujutusele tundlik HH ja VV kanali polarimeetriline faasivahe, mida on soovitatud ka varasemates töödes kasutada täiendava andmeallikana üleujutuste kaardistamisel. Käesolevas doktoritöös mõõdeti polarimeetrilise X-laineala tehisava-radari HH/VV faasivahe suurenemine üleujutuste tõttu erineva kõrgusega okas- ja lehtmetsas.

2013 a vegetatsiooniperioodil korraldati Rannu test-alal välimõõtmistega toetatud eksperiment uurimaks X- ja C-laineala polarimeetrilise ning X-laineala interferomeetrilise tehisava-radari parameetrite tundlikkust rohumaade tingimuste muutustele. Ilmnes, et ühepäevase vahega kogutud X-laineala tehisava-radari interferomeetriliste paaride koherentsus korreleerus rohu kõrgusega. Koherentsus oli seda madalam, mida kõrgem oli rohi - leitud seost on võimalik potentsiaalselt rakendada niitmise tuvastamiseks. TerraSAR-X ja RADARSAT-2 polarimeetriliste aegridade analüüsi tulemusel leiti kaks niitmisele tundlikku parameetrit: HH/VV polarimeetriline koherentsus ja polarimeetriline entroopia. Niitmise järel langes HH/VV polarimeetriline koherentsus järsult ning polarimeetriline entroopia tõusis järsult. Rohu tagasikasvamise faasis hakkas HH/VV polarimeetriline koherentsus aeglaselt kasvama ning entroopia aeglaselt kahanema. Täheldatud efekt oli tugevam TerraSAR-X X-laineala aegridadel kui RADARSAT-2 C-riba tehisava-radari mõõtmistel ning seda selgemini nähtav mida rohkem biomassi niitmise järgselt maha jäi. Leitud HH/VV polarimeetrilise koherentsuse ja polarimeetrilise entroopia käitumine vastas taimkatte osakestepilve radarikiirguse tagasihajumismudelile. Mudeli järgi põhjus-

tas eelnimetatud parameetrite iseloomulikku muutust rohukõrte kui dipoolide orientatsiooni ja korrastatuse muut niitmise tõttu, mis on kooskõlas meie välimõõtmiste andmetega.

ACKNOWLEDGEMENTS

First and foremost I would like to thank my supervisors Kaupo, Mart and Anu. Mart has been an unending source of energy and motivation, and I thank him and Kaupo for giving me the opportunity to have this journey in the first place. I am tremendously happy to have had the chance to work together with Kaupo who is a fantastic colleague. I am grateful for Anu's support throughout the years, and for creating the most excellent working conditions in Tõravere. I acknowledge the input and support from my colleagues from Aalto University and DLR Jaan Praks, Oleg Antropov and Thomas Jagdhuber.

I am happy I could share the journey with old and new friends. I thank Andris for many fun and serious moments throughout Ventspils and Tartu, Kaspars for unconditional friendship and support, Jānis and Inga for all the time we have spent together. I am thankful to Armands and Līga, Kate, Õie, Aire, Gatis, Kalev, Tanel, Shahab, Franz 'the Baron', Philipp, Frank, Dace and Alekss, Antons and Ilze, Rūta and Ģirts, Jānis and Aija, Tarvi, Juste, Rob, Chris, Jaan, Hendrik, Mihkel, Boris, David, Jouni, Petri, and other friends and colleagues from Tõravere and the ESTCube programme for support and their time.

My scientific journey started in Ventspils, and I am grateful to Juris Žagars for giving me the opportunity to start studying space technology and remote sensing in particular. I thank my colleagues form Ventspils University College Ance, Gundars, Mārtiņš, Juris, Inese, Linda, Inga, Gatis, Jānis, Miks, Ieva and others. You made my introduction to the scientific world fun and fulfilling. My thanks go to Valdis Avotiņš, Juris Roberts Kalniņš, and Normunds Jēkabsons for creating the conditions for my development in Ventspils.

I gratefully acknowledge the funding sources that enabled this PhD work. I was funded by the Archimedes Foundation under European Social Fund's Doctoral Studies and the Internationalization Program DoRa, and the Kristjan Jaak Program. The DoRa coordinator Kadri Orula is acknowledged for her administrative support.

Lastly, I would like to thank my family, Irina and Indulis, as well as my grandparents, for giving me the thirst for knowledge, and for supporting me in my pursuits. And most of all for my supportive and encouraging partner Kristiina whose patient support during this PhD work is very appreciated.

CURRICULUM VITAE

Personal data

Name	Karlis Zalite
Date, place of birth	22 July 1984, Riga, Latvia
Citizenship	Latvian
Marital status	unmarried
Current employment	Tartu Observatory (junior research associate)
Address	Tartu Observatory 61602 Tõravere Tartumaa, Estonia
Phone	(+371) 26 5519 841
E-mail	karlis.zalite@to.ee

Education

1991 – 1995	Riga High School Nr.36
1995 – 2002	Riga Centre Language School
2002 – 2005	Ventspils University College, undergraduate student, BSc 2003 (computer science)
2005 – 2007	Ventspils University College, graduate student, MSc 2005 (computer science)
2011 – 2016	University of Tartu, PhD student

Employment

2005 – 2007	Ventspils Digital Centre, client administrator
2007 – 2015	Ventspils University College, lecturer
2007 – 2009, 2010 – . . .	Ventspils International Radio Astronomy Centre, researcher
2009 – 2010	Ventspils Electronics Factory, process engineer
2011 – . . .	Tartu Observatory, junior research associate
2013 – 2014	University of Tartu, lecturer
2015	Aalto University, visiting researcher
2015 – . . .	Lund University, visiting researcher

Professional training

March 2006	Microsoft Approved Course 2710: Analyzing Requirements and Defining Microsoft .NET Solution Architectures, Riga, Latvia
September 2007	International Training Course on Management Skills and Intersectoral Mobility (Eesti Noorte Teadlaste Akadeemia), Tallinn, Estonia

Conference presentations

31.01.2011	Conference "69th conference of the University of Latvia", Riga, Latvia. *Oral presentation*: "Application of remote sensing in evaluating post-fire regeneration of Bazu mire"
07.05 – 08.05 2012	Conference "Baltic Applied Astroinformatics and Space data Processing", Ventspils, Latvia. *Oral presentation*: "The design of fault tolerant system for ESTCube-1"
28.01 – 01.02 2013	Conference "European Space Agency POLinSAR 2013 Workshop", Frascati, Italy. *Poster presentation*: "Effects of Inundated Vegetation Parameters on X-band HH-VV Backscatter"
15.05 – 16.05 2013	Conference "Baltic Applied Astroinformatics and Space data Processing", Ventspils, Latvia. *Oral presentation*: "Use of Polarimetric SAR to improve Detection of Flooded Vegetation"
28.01.2014	Conference "72nd conference of the University of Latvia", Riga, Latvia. *Oral presentation*: "Monitoring of grasslands with SAR X-band interferometric coherence"
07.05 – 08.05 2014	Conference "The Annual Exclusive Finnish-Estonian Remote Sensing Seminar", Toravere, Estonia. *Oral presentation*: "Monitoring of Estonian Grasslands with Repeat-Pass Interferometry"
13.07 – 18.07 2014	Conference "IEEE Geoscience and Remote Sensing Symposium", Quebec, Canada. *Oral presentation*: "Towards detecting mowing of agricultural grasslands from multi-temporal Cosmo-SkyMed data"
20.08 – 21.08 2015	Conference "Baltic Applied Astroinformatics and Space data Processing", Ventspils, Latvia.

Oral presentation: "Monitoring of agricultural grasslands using SAR Polarimetry and Interferometry: results from the Rannu 2013 campaign"

Language skills

Latvian	native
English	very good
Russian	very good
Estonian	basic

Honours and Awards

2011	DoRa 4 scholarship (SA Archimedes)
2014	Kristjan Jaak scholarship (SA Archimedes)
2015	DoRa 6 scholarship (SA Archimedes)

Fields of research

SAR remote sensing of grasslands.
Urban area mapping.

Publications

1. Pajusalu, M., Rantsus, R., Pelakauskas, M., Leitu, A., Ilbis, E., Kalde, J., Lillmaa, H., Reinumagi, R., Voormansik, K., **Zalite, K.**, et al., *Design of the Electrical Power System for the ESTCube-1 Satellite*, Latvian Journal of Physics and Technical Sciences. Volume 49, Issue 3, pp. 16–24, 2012
2. Voormansik, K., Praks, J., Antropov, O., Jagomagi, J., **Zalite, K.**, *Flood Mapping With TerraSAR-X in Forested Regions in Estonia*, IEEE Journal of Selected Topics in Applied Earth Observations and Remote Sensing, v.7-2, pp. 562-577, 2013
3. Olesk, A., Voormansik, K., Luud, A., Rennel, M., **Zalite, K.**, et al., *Countrywide Forest Biomass Estimates From PALSAR L-Band Backscatter To Improve Greenhouse Gas Inventory In Estonia*, Proc. of 6th Int. Workshop on Science and Applications of SAR Polarimetry and Polarimetric Interferometry - PolInSAR 2013, ESA SP-713, 2013
4. **Zalite, K.**, Voormansik, K., Olesk, A., et al., *Effects of Inundated Vegetation on X-Band HH-VV Backscatter and Phase Difference*, IEEE Journal of Selected Topics in Applied Earth Observations and Remote Sensing, v.7–4, pp. 1402–1406, 2014

5. Laizans, K, Sunter, I., **Zalite, K.**, et al., *Design of the fault tolerant command and data handling subsystem for ESTCube-1*, Proc. of the Estonian Academy of Sciences, v.63–2S, pp. 222–231, 2014
6. Latt, S., Slavinskis, A., Ilbis, E., Kvell, U., Voormansik, K., Kulu, E., Pajusalu, M., Kuuste, H., Sunter, I., Eenmae, T., Laizans, K., **Zalite, K.**, et al., *ESTCube-1 nanosatellite for electric solar wind sail in-orbit technology demonstration*, Proc. of the Estonian Academy of Sciences, v.63–2S, pp. 200–209, 2014
7. **Zalite, K.**, Voormansik, K., Praks, J., et al., *Towards detecting mowing of agricultural grasslands from multi-temporal COSMO-SkyMed data*, Proc. of Geoscience and Remote Sensing Symposium (IGARSS), 2014 IEEE International, pp. 5076–5079, 2014
8. Slavinskis, A., Pajusalu, M., Kuuste, H., Ilbis, E., Eenmae, T., Sunter, I., Laizans, K., Ehrpais, H., Liias, P., Kulu, E., Viru, J., Kalde, J., Kvell, U., Kutt, J., **Zalite, K.**, et al., *ESTCube-1 In-Orbit Experience and Lessons Learned*, IEEE A&E Systems Magazine, v.30–8, pp. 12–22, 2015
9. Koppel, K., **Zalite, K.**, Sisas, A., et al., *Sentinel-1 for urban area monitoring – analyzing loca–area statistics and interferometric coherence methods for buildings' detection*, Proc. of Geoscience and Remote Sensing Symposium (IGARSS), 2015 IEEE International, pp. 1175–1178, 2015
10. **Zalite, K.**, Antropov, O., Praks, J., et al., *Monitoring of Agricultural Grasslands with Time Series of X-band Repeat-Pass Interferometric SAR*, IEEE Journal of Selected Topics in Applied Earth Observations and Remote Sensing, vol. PP–99, pp. 1-11, 2015
11. Voormansik, K., Jagdhuber, T., **Zalite, K.**, et al., *Observations of Cutting Practices in Agricultural Grasslands using Polarimetric SAR*, IEEE Journal of Selected Topics in Applied Earth Observations and Remote Sensing, vol. PP-99, pp. 1–15, 2015

ELULOOKIRJELDUS

Isikuandmed

Nimi	Karlis Zalite
Sünniaeg ja -koht	22. juuli 1984, Riga, Läti
Kodakondsus	läti
Perekonnaseis	vallaline
Praegune töökoht	Tartu Observatoorium (nooremteadur)
Aadress	Tartu Observatoorium 61602 Tõravere Tartumaa, Eesti
Telefon	(+371) 26 5519 841
E-post	karlis.zalite@to.ee

Haridustee

1991 – 1995	Riia 36. keskkool
1995 – 2002	Kesk-Riia Keeltekool
2002 – 2005	Ventspilsi Kõrgkool, üliõpilane, BSc 2003 (arvutitehnika)
2005 – 2007	Ventspilsi Kõrgkool, magistrand, MSc 2005 (arvutitehnika)
2011 – 2016	Tartu Ülikool, doktorant

Teenistuskäik

2005 – 2007	Ventspilsi Digitaalkeskus, kliendiadministraator
2007 – 2015	Ventspilsi Kõrgkool, lektor
2007 – 2009, 2010 – . . .	Ventspilsi Rahvusvaheline Raadioastronoomia Keskus, teadur
2009 – 2010	Ventspilsi Elektroonikavabrik, inseneer
2011 – . . .	Tartu Observatoorium, nooremteadur
2013 – 2014	Tartu Ülikool, lektor
2015	Aalto Ülikool, külalisteadur
2015 – . . .	Lund Ülikool, külalisteadur

Täiendkoolitus

Märts 2006	Microsoft Approved Course 2710: Analyzing Requirements and Defining Microsoft .NET Solution Architectures, Riia, Läti
September 2007	International Training Course on Management Skills and Intersectoral Mobility (Eesti Noorte Teadlaste Akadeemia), Tallinn, Eesti

Konverentsid

31.01.2011	Konverents "69th conference of the University of Latvia", Riia, Läti. *Suuline ettekane*: "Application of remote sensing in evaluating post-fire regeneration of Bazu mire"
07.05 – 08.05 2012	Konverents "Baltic Applied Astroinformatics and Space data Processing", Ventspils, Läti. *Suuline ettekane*: "The design of fault tolerant system for ESTCube-1"
28.01 – 01.02 2013	Konverents "European Space Agency POLinSAR 2013 Workshop", Frascati, Itaalia. *Postri ettekane*: "Effects of Inundated Vegetation Parameters on X-band HH-VV Backscatter"
15.05 – 16.05 2013	Konverents "Baltic Applied Astroinformatics and Space data Processing", Ventspils, Läti. *Suuline ettekane*: "Use of Polarimetric SAR to improve Detection of Flooded Vegetation"
28.01.2014	Konverents "72nd conference of the University of Latvia", Riia, Läti. *Suuline ettekane*: "Monitoring of grasslands with SAR X-band interferometric coherence"
07.05 – 08.05 2014	Konverents "The Annual Exclusive Finnish-Estonian Remote Sensing Seminar", Tõravere, Eesti. *Suuline ettekane*: "Monitoring of Estonian Grasslands with Repeat-Pass Interferometry"
13.07 – 18.07 2014	Konverents "IEEE Geoscience and Remote Sensing Symposium", Quebec, Kanada. *Suuline ettekane*: "Towards detecting mowing of agricultural grasslands from multi-temporal Cosmo-SkyMed data"
20.08 – 21.08 2015	Konverents "Baltic Applied Astroinformatics and Space data Processing", Ventspils, Läti.

Suuline ettekane: “Monitoring of agricultural grasslands using SAR Polarimetry and Interferometry: results from the Rannu 2013 campaign”

Keelteoskus

läti keel	emakeel
inglise keel	väga hea
vene keel	väga hea
eesti keel	algtase

Uurimistoetused ja stipendiumid

2011	DoRa 4 stipendium (SA Archimedes)
2014	Kristjan Jaagu stipendium (SA Archimedes)
2015	DoRa 6 stipendium (SA Archimedes)

Peamised uurimissuunad

Tehisavaradar (*ing.* - SAR) rohumaade kaugseire.
Linnastumise kaardistamine ja seire.

Publikatsioonid

1. Pajusalu, M., Rantsus, R., Pelakauskas, M., Leitu, A., Ilbis, E., Kalde, J., Lillmaa, H., Reinumagi, R., Voormansik, K., **Zalite, K.**, et al., *Design of the Electrical Power System for the ESTCube-1 Satellite*, Latvian Journal of Physics and Technical Sciences. Volume 49, Issue 3, pp. 16–24, 2012
2. Voormansik, K., Praks, J., Antropov, O., Jagomagi, J., **Zalite, K.**, *Flood Mapping With TerraSAR-X in Forested Regions in Estonia*, IEEE Journal of Selected Topics in Applied Earth Observations and Remote Sensing, v.7-2, pp. 562-577, 2013
3. Olesk, A., Voormansik, K., Luud, A., Rennel, M., **Zalite, K.**, et al., *Countrywide Forest Biomass Estimates From PALSAR L-Band Backscatter To Improve Greenhouse Gas Inventory In Estonia*, Proc. of 6th Int. Workshop on Science and Applications of SAR Polarimetry and Polarimetric Interferometry - PolInSAR 2013, ESA SP-713, 2013
4. **Zalite, K.**, Voormansik, K., Olesk, A., et al., *Effects of Inundated Vegetation on X-Band HH-VV Backscatter and Phase Difference*, IEEE Journal of Selected Topics in Applied Earth Observations and Remote Sensing, v.7–4, pp. 1402–1406, 2014

5. Laizans, K, Sunter, I., **Zalite, K.**, et al., *Design of the fault tolerant command and data handling subsystem for ESTCube-1*, Proc. of the Estonian Academy of Sciences, v.63–2S, pp. 222–231, 2014
6. Latt, S., Slavinskis, A., Ilbis, E., Kvell, U., Voormansik, K., Kulu, E., Pajusalu, M., Kuuste, H., Sunter, I., Eenmae, T., Laizans, K., **Zalite, K.**, et al., *ESTCube-1 nanosatellite for electric solar wind sail in-orbit technology demonstration*, Proc. of the Estonian Academy of Sciences, v.63–2S, pp. 200–209, 2014
7. **Zalite, K.**, Voormansik, K., Praks, J., et al., *Towards detecting mowing of agricultural grasslands from multi-temporal COSMO-SkyMed data*, Proc. of Geoscience and Remote Sensing Symposium (IGARSS), 2014 IEEE International, pp. 5076–5079, 2014
8. Slavinskis, A., Pajusalu, M., Kuuste, H., Ilbis, E., Eenmae, T., Sunter, I., Laizans, K., Ehrpais, H., Liias, P., Kulu, E., Viru, J., Kalde, J., Kvell, U., Kutt, J., **Zalite, K.**, et al., *ESTCube-1 In-Orbit Experience and Lessons Learned*, IEEE A&E Systems Magazine, v.30–8, pp. 12–22, 2015
9. Koppel, K., **Zalite, K.**, Sisas, A., et al., *Sentinel-1 for urban area monitoring – analyzing loca–area statistics and interferometric coherence methods for buildings' detection*, Proc. of Geoscience and Remote Sensing Symposium (IGARSS), 2015 IEEE International, pp. 1175–1178, 2015
10. **Zalite, K.**, Antropov, O., Praks, J., et al., *Monitoring of Agricultural Grasslands with Time Series of X-band Repeat-Pass Interferometric SAR*, IEEE Journal of Selected Topics in Applied Earth Observations and Remote Sensing, vol. PP–99, pp. 1-11, 2015
11. Voormansik, K., Jagdhuber, T., **Zalite, K.**, et al., *Observations of Cutting Practices in Agricultural Grasslands using Polarimetric SAR*, IEEE Journal of Selected Topics in Applied Earth Observations and Remote Sensing, vol. PP-99, pp. 1–15, 2015

DISSERTATIONES PHYSICAE UNIVERSITATIS TARTUENSIS

1. **Andrus Ausmees.** XUV-induced electron emission and electron-phonon interaction in alkali halides. Tartu, 1991.
2. **Heiki Sõnajalg.** Shaping and recalling of light pulses by optical elements based on spectral hole burning. Tartu, 1991.
3. **Sergei Savihhin.** Ultrafast dynamics of F-centers and bound excitons from picosecond spectroscopy data. Tartu, 1991.
4. **Ergo Nõmmiste.** Leelishalogeniidide röntgenelektronemissioon kiiritamisel footonitega energiaga 70–140 eV. Tartu, 1991.
5. **Margus Rätsep.** Spectral gratings and their relaxation in some low-temperature impurity-doped glasses and crystals. Tartu, 1991.
6. **Tõnu Pullerits.** Primary energy transfer in photosynthesis. Model calculations. Tartu, 1991.
7. **Olev Saks.** Attoampri diapasoonis voolude mõõtmise füüsikalised alused. Tartu, 1991.
8. **Andres Virro.** AlGaAsSb/GaSb heterostructure injection lasers. Tartu, 1991.
9. **Hans Korge.** Investigation of negative point discharge in pure nitrogen at atmospheric pressure. Tartu, 1992.
10. **Jüri Maksimov.** Nonlinear generation of laser VUV radiation for high-resolution spectroscopy. Tartu, 1992.
11. **Mark Aizengendler.** Photostimulated transformation of aggregate defects and spectral hole burning in a neutron-irradiated sapphire. Tartu, 1992.
12. **Hele Siimon.** Atomic layer molecular beam epitaxy of A^2B^6 compounds described on the basis of kinetic equations model. Tartu, 1992.
13. **Tõnu Reinot.** The kinetics of polariton luminescence, energy transfer and relaxation in anthracene. Tartu, 1992.
14. **Toomas Rõõm.** Paramagnetic H^{2-} and F^+ centers in CaO crystals: spectra, relaxation and recombination luminescence. Tallinn, 1993.
15. **Erko Jalviste.** Laser spectroscopy of some jet-cooled organic molecules. Tartu, 1993.
16. **Alvo Aabloo.** Studies of crystalline celluloses using potential energy calculations. Tartu, 1994.
17. **Peeter Paris.** Initiation of corona pulses. Tartu, 1994.
18. **Павел Рубин.** Локальные дефектные состояния в CuO_2 плоскостях высокотемпературных сверхпроводников. Тарту, 1994.
19. **Olavi Ollikainen.** Applications of persistent spectral hole burning in ultrafast optical neural networks, time-resolved spectroscopy and holographic interferometry. Tartu, 1996.
20. **Ülo Mets.** Methodological aspects of fluorescence correlation spectroscopy. Tartu, 1996.
21. **Mikhail Danilkin.** Interaction of intrinsic and impurity defects in CaS:Eu luminophors. Tartu, 1997.

22. **Ирина Кудрявцева.** Создание и стабилизация дефектов в кристаллах KBr, KCl, RbCl при облучении ВУФ-радиацией. Тарту, 1997.
23. **Andres Osvet.** Photochromic properties of radiation-induced defects in diamond. Tartu, 1998.
24. **Jüri Örd.** Classical and quantum aspects of geodesic multiplication. Tartu, 1998.
25. **Priit Sarv.** High resolution solid-state NMR studies of zeolites. Tartu, 1998.
26. **Сергей Долгов.** Электронные возбуждения и дефектообразование в некоторых оксидах металлов. Тарту, 1998.
27. **Kaupo Kukli.** Atomic layer deposition of artificially structured dielectric materials. Tartu, 1999.
28. **Ivo Heinmaa.** Nuclear resonance studies of local structure in $RBa_2Cu_3O_{6+x}$ compounds. Tartu, 1999.
29. **Aleksander Shelkan.** Hole states in CuO_2 planes of high temperature superconducting materials. Tartu, 1999.
30. **Dmitri Nevedrov.** Nonlinear effects in quantum lattices. Tartu, 1999.
31. **Rein Ruus.** Collapse of 3d (4f) orbitals in 2p (3d) excited configurations and its effect on the x-ray and electron spectra. Tartu, 1999.
32. **Valter Zazubovich.** Local relaxation in incommensurate and glassy solids studied by Spectral Hole Burning. Tartu, 1999.
33. **Indrek Reimand.** Picosecond dynamics of optical excitations in GaAs and other excitonic systems. Tartu, 2000.
34. **Vladimir Babin.** Spectroscopy of exciton states in some halide macro- and nanocrystals. Tartu, 2001.
35. **Toomas Plank.** Positive corona at combined DC and AC voltage. Tartu, 2001.
36. **Kristjan Leiger.** Pressure-induced effects in inhomogeneous spectra of doped solids. Tartu, 2002.
37. **Helle Kaasik.** Nonperturbative theory of multiphonon vibrational relaxation and nonradiative transitions. Tartu, 2002.
38. **Tõnu Laas.** Propagation of waves in curved spacetimes. Tartu, 2002.
39. **Rünno Lõhmus.** Application of novel hybrid methods in SPM studies of nanostructural materials. Tartu, 2002.
40. **Kaido Reivelt.** Optical implementation of propagation-invariant pulsed free-space wave fields. Tartu, 2003.
41. **Heiki Kasemägi.** The effect of nanoparticle additives on lithium-ion mobility in a polymer electrolyte. Tartu, 2003.
42. **Villu Repän.** Low current mode of negative corona. Tartu, 2004.
43. **Алексей Котлов.** Оксианионные диэлектрические кристаллы: зонная структура и электронные возбуждения. Tartu, 2004.
44. **Jaak Talts.** Continuous non-invasive blood pressure measurement: comparative and methodological studies of the differential servo-oscillometric method. Tartu, 2004.
45. **Margus Saal.** Studies of pre-big bang and braneworld cosmology. Tartu, 2004.

46. **Eduard Gerškevitš.** Dose to bone marrow and leukaemia risk in external beam radiotherapy of prostate cancer. Tartu, 2005.
47. **Sergey Shchemelyov.** Sum-frequency generation and multiphoton ionization in xenon under excitation by conical laser beams. Tartu, 2006.
48. **Valter Kiisk.** Optical investigation of metal-oxide thin films. Tartu, 2006.
49. **Jaan Aarik.** Atomic layer deposition of titanium, zirconium and hafnium dioxides: growth mechanisms and properties of thin films. Tartu, 2007.
50. **Astrid Rekker.** Colored-noise-controlled anomalous transport and phase transitions in complex systems. Tartu, 2007.
51. **Andres Punning.** Electromechanical characterization of ionic polymer-metal composite sensing actuators. Tartu, 2007.
52. **Indrek Jõgi.** Conduction mechanisms in thin atomic layer deposited films containing TiO_2. Tartu, 2007.
53. **Aleksei Krasnikov.** Luminescence and defects creation processes in lead tungstate crystals. Tartu, 2007.
54. **Küllike Rägo.** Superconducting properties of MgB_2 in a scenario with intra- and interband pairing channels. Tartu, 2008.
55. **Els Heinsalu.** Normal and anomalously slow diffusion under external fields. Tartu, 2008.
56. **Kuno Kooser.** Soft x-ray induced radiative and nonradiative core-hole decay processes in thin films and solids. Tartu, 2008.
57. **Vadim Boltrushko.** Theory of vibronic transitions with strong nonlinear vibronic interaction in solids. Tartu, 2008.
58. **Andi Hektor.** Neutrino Physics beyond the Standard Model. Tartu, 2008.
59. **Raavo Josepson.** Photoinduced field-assisted electron emission into gases. Tartu, 2008.
60. **Martti Pärs.** Study of spontaneous and photoinduced processes in molecular solids using high-resolution optical spectroscopy. Tartu, 2008.
61. **Kristjan Kannike.** Implications of neutrino masses. Tartu, 2008.
62. **Vigen Issahhanjan.** Hole and interstitial centres in radiation-resistant MgO single crystals. Tartu, 2008.
63. **Veera Krasnenko.** Computational modeling of fluorescent proteins. Tartu, 2008.
64. **Mait Müntel.** Detection of doubly charged higgs boson in the CMS detector. Tartu, 2008.
65. **Kalle Kepler.** Optimisation of patient doses and image quality in diagnostic radiology. Tartu, 2009.
66. **Jüri Raud.** Study of negative glow and positive column regions of capillary HF discharge. Tartu, 2009.
67. **Sven Lange.** Spectroscopic and phase-stabilisation properties of pure and rare-earth ions activated ZrO_2 and HfO_2. Tartu, 2010.
68. **Aarne Kasikov.** Optical characterization of inhomogeneous thin films. Tartu, 2010.
69. **Heli Valtna-Lukner.** Superluminally propagating localized optical pulses. Tartu, 2010.

70. **Artjom Vargunin.** Stochastic and deterministic features of ordering in the systems with a phase transition. Tartu, 2010.
71. **Hannes Liivat.** Probing new physics in e+e− annihilations into heavy particles via spin orientation effects. Tartu, 2010.
72. **Tanel Mullari.** On the second order relativistic deviation equation and its applications. Tartu, 2010.
73. **Aleksandr Lissovski.** Pulsed high-pressure discharge in argon: spectroscopic diagnostics, modeling and development. Tartu, 2010.
74. **Aile Tamm.** Atomic layer deposition of high-permittivity insulators from cyclopentadienyl-based precursors. Tartu, 2010.
75. **Janek Uin.** Electrical separation for generating standard aerosols in a wide particle size range. Tartu, 2011.
76. **Svetlana Ganina.** Hajusandmetega ülesanded kui üks võimalus füüsikaõppe efektiivsuse tõstmiseks. Tartu, 2011
77. **Joel Kuusk.** Measurement of top-of-canopy spectral reflectance of forests for developing vegetation radiative transfer models. Tartu, 2011.
78. **Raul Rammula**. Atomic layer deposition of HfO_2 – nucleation, growth and structure development of thin films. Tartu, 2011.
79. **Сергей Наконечный.** Исследование электронно-дырочных и интерстициал-вакансионных процессов в монокристаллах MgO и LiF методами термоактивационной спектроскопии. Тарту, 2011.
80. **Niina Voropajeva.** Elementary excitations near the boundary of a strongly correlated crystal. Tartu, 2011.
81. **Martin Timusk.** Development and characterization of hybrid electro-optical materials. Tartu, 2012, 106 p.
82. **Merle Lust.** Assessment of dose components to Estonian population. Tartu, 2012, 84 p.
83. **Karl Kruusamäe.** Deformation-dependent electrode impedance of ionic electromechanically active polymers. Tartu, 2012, 128 p.
84. **Liis Rebane.** Measurement of the $W \to \tau\nu$ cross section and a search for a doubly charged Higgs boson decaying to τ-leptons with the CMS detector. Tartu, 2012, 156 p.
85. **Jevgeni Šablonin.** Processes of structural defect creation in pure and doped MgO and NaCl single crystals under condition of low or super high density of electronic excitations. Tartu, 2013, 145 p.
86. **Riho Vendt**. Combined method for establishment and dissemination of the international temperature scale. Tartu, 2013, 108 p.
87. **Peeter Piksarv.** Spatiotemporal characterization of diffractive and non-diffractive light pulses. Tartu, 2013, 156 p.
88. **Anna Šugai.** Creation of structural defects under superhigh-dense irradiation of wide-gap metal oxides. Tartu, 2013, 108 p.
89. **Ivar Kuusik.** Soft X-ray spectroscopy of insulators. Tartu, 2013, 113 p.
90. **Viktor Vabson**. Measurement uncertainty in Estonian Standard Laboratory for Mass. Tartu, 2013, 134 p.

91. **Kaupo Voormansik.** X-band synthetic aperture radar applications for environmental monitoring. Tartu, 2014, 117 p.
92. **Deivid Pugal.** hp-FEM model of IPMC deformation. Tartu, 2014, 143 p.
93. **Siim Pikker.** Modification in the emission and spectral shape of photostable fluorophores by nanometallic structures. Tartu, 2014, 98 p.
94. **Mihkel Pajusalu**. Localized Photosynthetic Excitons. Tartu, 2014, 183 p.
95. **Taavi Vaikjärv.** Consideration of non-adiabaticity of the Pseudo-Jahn-Teller effect: contribution of phonons. Tartu, 2014, 129 p.
96. **Martin Vilbaste.** Uncertainty sources and analysis methods in realizing SI units of air humidity in Estonia. Tartu, 2014, 111 p.
97. **Mihkel Rähn.** Experimental nanophotonics: single-photon sources- and nanofiber-related studies. Tartu, 2015, 107 p.
98. **Raul Laasner.** Excited state dynamics under high excitation densities in tungstates. Tartu, 2015, 125 p.
99. **Andris Slavinskis.** EST Cube-1 attitude determination. Tartu, 2015, 104 p.